

Synthesis of the Seismic Structure of the Greater Alaska Region: Continental Lithosphere

Xiaotao Yang¹, Michael Everett Mann², Karen M. Fischer², Margarete Jadamec^{3,4}, S. Shawn Wei⁵, Gary L. Pavlis⁶, and Andrew Schaeffer⁷

¹Department of Earth, Atmospheric, and Planetary Sciences, Purdue University, West Lafayette, IN, USA.

²Department of Earth, Environmental, and Planetary Sciences, Brown University, Providence, Rhode Island, USA.

³Department of Geology, University at Buffalo, SUNY, Buffalo, New York, USA.

⁴Institute for Artificial Intelligence and Data Science, University at Buffalo, SUNY, Buffalo, New York, USA.

⁵Department of Earth and Environmental Sciences, Michigan State University, East Lansing, MI, USA.

⁶Department of Earth and Atmospheric Sciences, Indiana University Bloomington, Bloomington, IN, USA.

⁷Geological Survey of Canada Pacific Division, Sidney Subdivision, Natural Resources Canada, Sidney, BC, CA.

17 Abstract

18 Significant advances have been made over the last two decades in constraining the structure
19 of the continental lithosphere in Alaska, particularly with the EarthScope USArray seismic
20 data collection efforts. This paper distills recent seismic models in Alaska and western Yukon
21 (Canada) and relates them to major faults and tectonic terranes. We synthesize results from
22 eight shear-wave velocity models and seven crustal thickness models. Through objective
23 clustering of seismic velocity profiles, we identify six different velocity domains, separately
24 for the crust (at the depth range of 10-50 km) and the mantle (at the depth range of 40-120
25 km). The crustal seismic domains show strong correlations with average crustal thickness
26 patterns and the distribution of major faults and tectonic terranes. The mantle seismic
27 velocity domains demonstrate signatures of major faults and tectonic terranes in northern
28 Alaska, while in southern Alaska the domains are primarily controlled by the geometry of
29 the subducting lithosphere. The results of this study have significant implications for the
30 tectonics and geodynamics of the overriding continental lithosphere from the margin to the
31 interior. This synthesis will be of interest to future studies of Alaska as well as other modern
32 and ancient systems involving convergent margins and terrane accretions.

33 **1 Introduction**

34 Geologic observations over the past 40 years suggest that the Alaskan lithosphere has
 35 been assembled from a collage of fragments since the Mesozoic (W. J. Nokleberg et al.,
 36 1994; Plafker & Berg, 1994; Silberling et al., 1994; Colpron et al., 2007). These fragments
 37 make Alaska a type locality for the concept of terrane accretion (Coney et al., 1980; Colpron
 38 et al., 2007; Moore & Box, 2016; T. L. Pavlis et al., 2019). New seismic imaging results
 39 during the past two decades or so have provided fundamental constraints on the lithospheric
 40 structure of Alaska. In this study, we seek to shed new light on the structure of the con-
 41 tinental lithosphere in Alaska and northwesternmost Canada by integrating the results of
 42 recent shear-wave velocity models and receiver function studies enabled by data from the
 43 EarthScope Transportable Array (TA). In this paper, EarthScope refers to the U.S. Na-
 44 tional Science Foundation program operated from 2003 to 2018. Our study area lies within
 45 a broad tectonic region that spans the southern margin, where the Pacific plate subducts
 46 beneath the North American plate, northward to the interior and the North Slope of Alaska
 47 (Figure 1a). From west to east, this convergent margin transitions from ocean-ocean sub-
 48 duction approximately west of 166°W longitude (DeMets et al., 1994; Bird, 2003; Tozer
 49 et al., 2019; Müller et al., 2019; Seton et al., 2020), through ocean-continent subduction
 50 between approximately 166°W to 144°W longitude (Plafker, Moore, & Winkler, 1994; Bird,
 51 2003; Jadamec & Billen, 2010; Tozer et al., 2019; Müller et al., 2019; Seton et al., 2020), to
 52 a subduction-collision zone from approximately 144°W to 137°W longitude (Enkelmann et
 53 al., 2010; Koons et al., 2010; Elliott & Freymueller, 2020). In northern Alaska, the overrid-
 54 ing lithosphere transitions from continental to oceanic, through a modern passive margin
 55 that leads into the Arctic Ocean and the Canada Basin (Grantz et al., 1994; Tozer et al.,
 56 2019; Müller et al., 2019; Seton et al., 2020).

57 This study focuses on the lithosphere of mainland Alaska and the western Yukon re-
 58 gion. This region is comprised of a series of amalgamated tectonic terranes and large-scale
 59 faults (Figure 1b; Plafker & Berg, 1994; Colpron et al., 2007; Koehler & Carver, 2018). Some
 60 of the major fault systems in the study area include the Kobuk Fault Zone along the
 61 southern border of the Brooks Range in northern Alaska, the Kaltag and Tintina Faults
 62 in central Alaska, and the Denali Fault System in southcentral Alaska (Plafker, Gilpin, &
 63 Lahr, 1994). These faults are primarily parallel to the arcuate plate margin (Figure 1b;
 64 Colpron et al., 2007). In addition, there are smaller-scale southwest-northeast trending
 65 faulting features, such as the Nixon Fork-Iditarod Fault and the Porcupine Shear Zone. For
 66 tectonic terranes, the Arctic Alaska terrane, with three subterranea, occupies most of the
 67 area north of the Kobuk Fault Zone and the Seward Peninsula. Western Alaska is domi-
 68 nated by the continental arc setting Koyukuk terrane and the accreted continental margin
 69 setting Farewell terrane (Figure 1b; Colpron et al., 2007). Eastern Alaska contains mostly
 70 the North America platformal and basinal terranes (Figure 1b; Colpron et al., 2007). The
 71 Wrangellia composite terrane dominates the Alaska region south of the Denali Fault Sys-
 72 tem with accreted and displaced subterranea (Coney et al., 1980; Falkowski & Enkelmann,
 73 2016). There are numerous fundamental questions remaining regarding the structure and
 74 tectonics of the continental lithosphere in the Greater Alaska region. Given Alaska's his-
 75 tory of terrane accretion, how do the terrane boundaries and related faults correlate with
 76 present-day crustal and mantle lithospheric structure? How strongly does the geologic his-
 77 tory of a terrane control its present-day crustal structure? How deep do the signatures of
 78 terrane accretion extend into the mantle lithosphere? What is the impact of the subducting-
 79 colliding Yakutat Microplate on the structure of the overriding plate? Understanding these
 80 questions requires comprehensive and objective knowledge about the deep structure of the
 81 lithosphere, building on top of the discovery from surface geology and tectonic studies. This
 82 motivates us to examine the relationship between crustal and mantle seismic structures and
 83 major faults and tectonic terranes.

84 The data from the EarthScope TA, together with other concurrent temporary seismic
 85 networks, have provided new constraints on the seismic and tectonic structure of the con-

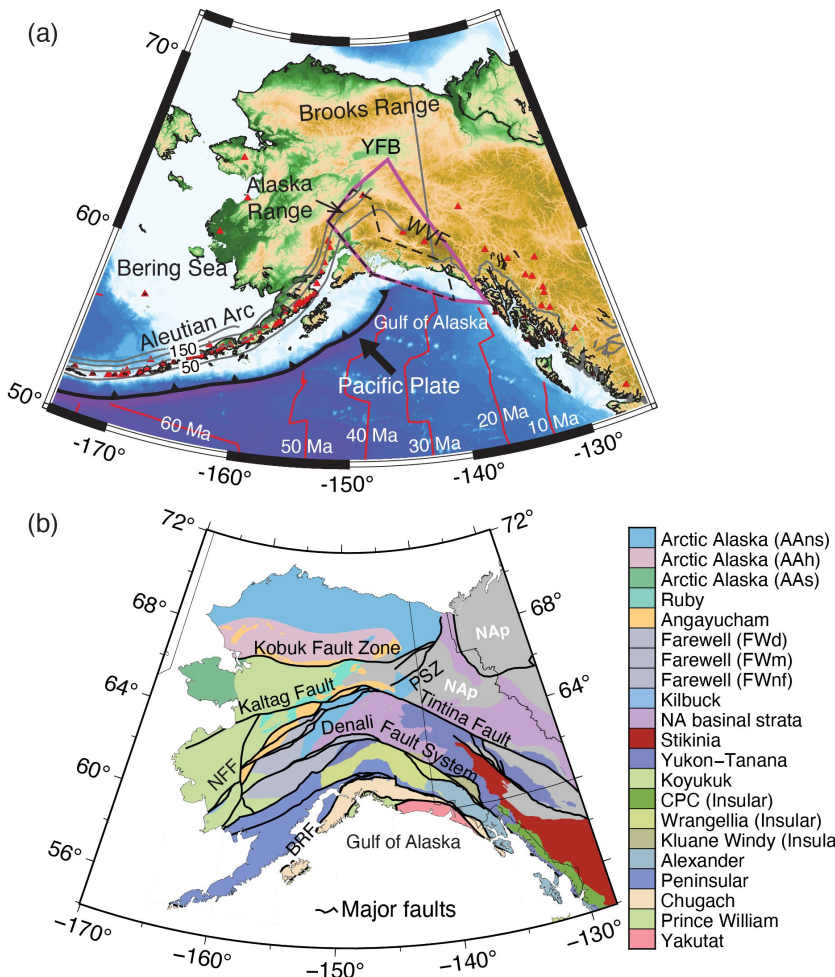


Figure 1. Tectonic settings of Alaska. (a) Key tectonic settings of Alaska, including the subduction of the Pacific Plate and the Yakutat microplate along the curved margin. Major topographic features are labels, including the Alaska Range, the Brooks Range, the Yukon Flats Basin (YFB), and the Wrangell Volcanic Field (WVF). The slab depth contours are from Slab2.0 (Hayes et al., 2018). The ages of the Pacific Plate are from Seton et al. (2020). The dashed black and solid magenta polygons mark the outlines of the Yakutat Microplate, the existence of which was originally proposed by Plafker et al. (1978), from Eberhart-Phillips et al. (2006) and G. L. Pavlis et al. (2019), respectively. Red triangles are active volcanoes. (b) Major terranes (color-shaded areas) and faults (thick lines) of the Canadian-Alaskan cordillera from Colpron et al. (2007). Fault labels: PSZ - Porcupine Shear Zone, NFF - Nixon Fork-Iditarod Fault, BRF - Border Range Fault. Terrane labels: AAns - Arctic Alaska North Slope subterrane, AAh - Arctic Alaska Hammond-Coldfoot subterrane, AAs - Arctic Alaska Seward subterrane, FWd - Farewell Dillinger subterrane, FWm - Farewell Mystic subterrane, FWnf - Farewell Nixon Fork subterrane, CPC - Coast Plutonic Complex, NAp - North America platformal strata in western Laurentia.

tinental United States and Alaska. From 2005 to 2015 the TA was deployed across the contiguous United States from the active tectonic boundary in the west to the passive continental margin on the east coast. In 2015, the USArray Transportable Array began moving instruments to Alaska and westernmost Canada. This has dramatically improved the seis-

mic data coverage in Alaska and western Yukon (Canada). Benefiting from the USArray TA records, there have been several seismic velocity and discontinuity models published in the past decade or so using different methods, parameters, and types of data (e.g., Ward & Lin, 2018; Jiang et al., 2018; Martin-Short et al., 2018; Gou et al., 2019; Feng & Ritzwoller, 2019; Berg et al., 2020; Yang & Gao, 2020; Esteve et al., 2020; Audet et al., 2019; Nayak et al., 2020; Esteve et al., 2021; Gama et al., 2022b; Liu et al., 2022; Veenstra et al., 2006; Rossi et al., 2006; Zhang et al., 2019; Mann et al., 2022; Ai et al., 2005; Rondenay et al., 2008, 2010; Kim et al., 2014; Brennan et al., 2011; Allam et al., 2017; Gama et al., 2022a; Haney et al., 2020). While sharing major seismic features, different models also reveal some unique seismic features that are only observed in certain models or a subset of the models. The inconsistency in seismic features among different models leads to uncertainties in characterizing coherent structural constraints and hinders the understanding of the geology and tectonics of Alaska. In this paper, we present a synthesis of seismic studies that utilize the seismic records from the EarthScope stations, focusing on extracting objective constraints from these results on the seismic structure of the lithosphere of the region. By combining eight shear-wave velocity models and seven crustal thickness models, we identify six different seismic domains, separately for the crust (at the depth range of 10–50 km) and the mantle lithosphere (at the depth range of 40–120 km). The crustal seismic domains show strong correlations with major faults and tectonic terranes. The mantle seismic domains demonstrate signatures of major faults and tectonic terranes in northern Alaska with a prominent reflection of the subduction structure in central and southern Alaska. The results of this study have significant implications for the tectonics and geodynamics of the overriding continental lithosphere from the margin to the interior.

2 Data: compilation of seismic models

The study area spans the region from the subduction zone along the southern Alaska margin to the North Slope of Alaska bordering the Arctic Ocean. We focus on two types of seismic results for Alaska: 1) 3-D shear-wave velocity models of the crust and uppermost mantle, and 2) thicknesses of the overriding crust. We exclude results that only cover the footprint of the Alaska Amphibious Community Seismic Experiment (Barchek et al., 2020). We attempt to reveal common features in the models we used but not to compare and contrast detailed interpretations different authors made from their individual models. The readers are encouraged to read the corresponding publications summarized in Tables 1 and 2 for detailed descriptions of each individual seismic model we used. The seismic models synthesized in this study benefit from the data recorded by 29 seismic networks, as shown in Figure 2a. The network codes include 5C, 7C, AK, AT, AV, CN, II, IM, IU, PN, PO, PP, TA, US, XE, XF, XL, XM, XN, XO, XR, XV, XY, XZ, YE, YG, YM, YO, YV, Z5, and ZE. See **Availability Statement** and Table S1 in the online supplement for the descriptions and references corresponding to these network codes.

2.1 3-D shear-wave velocity models

We collected eight representative 3-D shear-wave velocity models. Since the arrival of the EarthScope TA in Alaska, there have been a large number of velocity models published using data from the EarthScope TA stations and the Alaska regional network stations (e.g., Ward & Lin, 2018; Jiang et al., 2018; Martin-Short et al., 2018; Gou et al., 2019; Feng & Ritzwoller, 2019; Berg et al., 2020; Yang & Gao, 2020; Esteve et al., 2020; Audet et al., 2019; Nayak et al., 2020; Esteve et al., 2021; Gama et al., 2022b; Liu et al., 2022). To narrow down the velocity models for this synthesis work, we select velocity models that satisfy the following conditions: 1) covers most of mainland Alaska, 2) provides isotropic seismic velocities, 3) uses part or all EarthScope TA data, 4) includes surface wave data to aid with the vertical resolution, 5) is available as a digital velocity model through IRIS Earth Model Collaboration or personal communications, 6) provides absolute velocities or perturbations with an explicitly known reference model, and 7) covers at least the continental

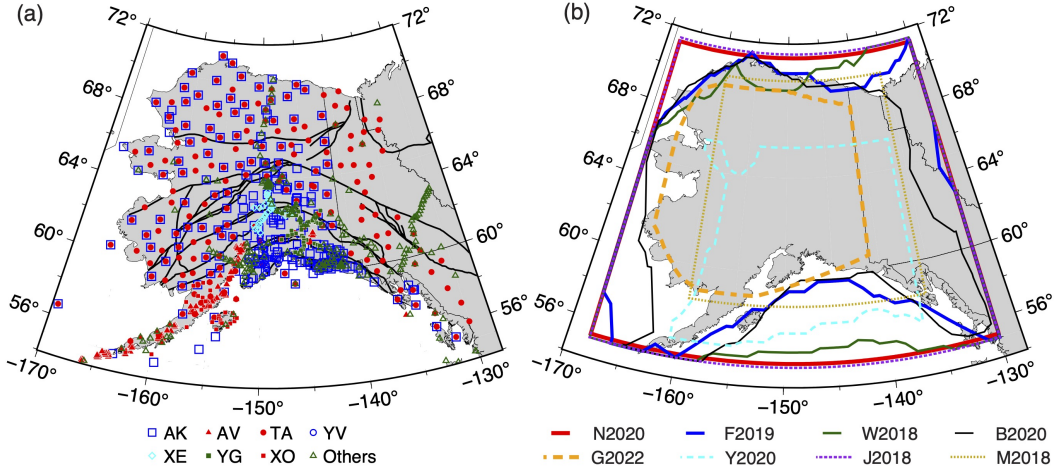


Figure 2. Seismic stations in Alaska and coverage of the seismic velocity models synthesized in this study. (a) Seismic stations from 29 networks between 2000 and 2022 that are used by the synthesized seismic models in this study. The station information is available through the IRIS Data Management Center and the International Federation of Digital Seismograph Networks. For simplicity in plotting, we plot the top seven networks, with the most stations, using different colors and symbols. Please see Table S1 in the supplement for the descriptions and references of all seismic networks plotted here. The thick lines are major fault traces as in Figure 1b. (b) Outlines of the shear-wave velocity models that are defined as regions with available shear-wave velocities between 1 km/s and 6 km/s. We use this velocity range to exclude unconstrained model grids. The outlines are estimated using the velocity model at the depth of about 30 km for all models. W2018 - model by Ward and Lin (2018), J2018 - model by Jiang et al. (2018), M2018 - model by Martin-Short et al. (2018), F2019 - model by Feng and Ritzwoller (2019), B2020 - model by Berg et al. (2020), Y2020 - model by Yang and Gao (2020), N2020 - model by Nayak et al. (2020), G2022 - model by Gama et al. (2022b). See Table 1 for more information about these velocity models.

141 crust in depth. With these criteria, we choose eight 3-D shear-wave velocity models using
 142 different datasets and imaging methods. The data types and tomographic imaging methods
 143 for all selected models are summarized in Table 1. Hereafter, we refer to these models
 144 with the labels as in Table 1. For simplicity and consistency in descriptions, we label each
 145 of the velocity models systematically with the initial of the last name of the first author
 146 and the year the model was published. Model F2019 (Feng & Ritzwoller, 2019) provides
 147 the vertically polarized shear-wave velocity, V_{SV} , and the radial anisotropy (in %), ξ . We
 148 compute the isotropic velocity, V_S , as the Voigt average of V_{SV} and horizontally (V_{SH})
 149 polarized shear-wave velocities (Anderson, 1987), which can be expressed as

$$V_S = \sqrt{2V_{SV}^2/3 + V_{SH}^2/3}. \quad (1)$$

150 The radial anisotropy, ξ , can be derived using

$$\xi = 100(V_{SH} - V_{SV})/V_{SV}. \quad (2)$$

151 From Equation 2, we have

$$V_{SH} = (0.01\xi + 1)V_{SV}. \quad (3)$$

152 Substituting Equation 3 into Equation 1, we get

$$V_S = \sqrt{\frac{2V_{SV}^2 + (0.01\xi + 1)^2V_{SV}^2}{3}}. \quad (4)$$

153 Using Equation 4, we could compute the isotropic velocity model with given V_{SV} and ξ .

154 The footprint of these stations covers the entire mainland Alaska region and the western
 155 Yukon (Canada) region. The EarthScope TA stations have a nominal spacing of about 85
 156 km, while some places, such as central Alaska and the Wrangell Volcanic Field, are covered
 157 with denser regional arrays. Among the eight velocity models, the Y2020 model (Yang &
 158 Gao, 2020) covers only central and southern Alaska (Figure 2b) while the M2018 (Martin-
 159 Short et al., 2018) and G2022 (Gama et al., 2022b) models cover most of Alaska. The rest
 160 of the velocity models cover the entire Alaska region. The J2018 (Jiang et al., 2018), F2019
 161 (Feng & Ritzwoller, 2019), B2020 (Berg et al., 2020), and N2020 (Nayak et al., 2020) models
 162 also cover western Yukon, Canada (Figure 2b). In addition to the uneven coverage, these
 163 velocity model files are all in different model grids with different grid spacing and ranges.
 164 To facilitate quantitative comparisons, we interpolate all velocity models onto the same 3-D
 165 grids with grid sizes of 0.2 and 0.1 in longitudinal and latitudinal directions and 2 km in
 166 depth. The choice of grid spacing is based on a trade-off between efficiency and the precision
 167 of cluster boundaries. When interpolating, we keep the maximum resolvable depth of the
 168 original model (Table 1).

169 Most of the selected velocity models share similar large-scale features showing the
 170 change of velocity structures from the subduction margin to the south, through the continental
 171 interior, to the passive margin to the north (Figures 3 and 4). At the depth of 24
 172 km (Figure 3), most of the velocity models show low-velocity features below the Brooks
 173 Range in northern Alaska and higher velocities to the south in central Alaska (Figure 3a-b,
 174 d-e, and g-h). The models also consistently show relatively low velocities in western and
 175 eastern Alaska, and western Yukon (Canada). These velocity features can also be observed
 176 from M2018 (Figure 3c), though the overall velocity variation is much smaller than in other
 177 models. Y2020 doesn't cover the Brooks Range, though the increase in velocity from the
 178 southern margin to the interior is seen (Figure 3f). At the depth of 80 km (Figure 4), all
 179 velocity models show elongated high-velocity features parallel to the Aleutian volcano arc,
 180 corresponding to the subducting Pacific plate. However, these high-velocity features possess
 181 different velocities and are in different scales. The slab-like high-velocity features have
 182 lower amplitudes in model M2018 and are less well-resolved horizontally in G2022. The
 183 upper mantle velocities in central Alaska are generally lower than the surrounding areas,
 184 particularly those north of the Kobuk Fault Zone below the Brooks Range and further north.
 185 Relatively high upper mantle velocities are shown in northeastern Alaska and western Yukon
 186 (Canada) in all models.

187 2.2 Crustal thickness models

188 Crustal thickness is a fundamental parameter in Earth science. In the analysis described
 189 in this section and the dataset provided with this paper, crustal thickness is defined as the
 190 difference between the Earth's surface and a nearly ubiquitous vertically-localized velocity
 191 increase, i.e., the Mohorovičić Discontinuity (Moho), located somewhere within the upper
 192 70 km of the Earth. Across Alaska, crustal thickness has been studied using seismic analyses
 193 for decades (e.g., Woppard et al., 1960; Fuis et al., 2008; Zhang et al., 2019). However, the
 194 recent TA deployment has greatly improved the coverage for estimating crustal thickness
 195 and allows for continuous analysis across the entire state. Here we compare crustal thickness
 196 estimates across Alaska from various studies and combine a number of them to create an
 197 integrated crustal thickness dataset for the region. We select and integrate the results
 198 from seven studies (Table 2) that explicitly measure crustal thickness across Alaska by
 199 determining the depth to a sharp velocity gradient, i.e., the Moho. The results from the
 200 selected studies can be split into two groups: single-station and multi-station estimates of
 201 crustal thicknesses (Table 2).

202 The single-station estimates (Veenstra et al., 2006; Rossi et al., 2006; Zhang et al.,
 203 2019; Mann et al., 2022) and an updated version of the crustal thicknesses of (Miller &

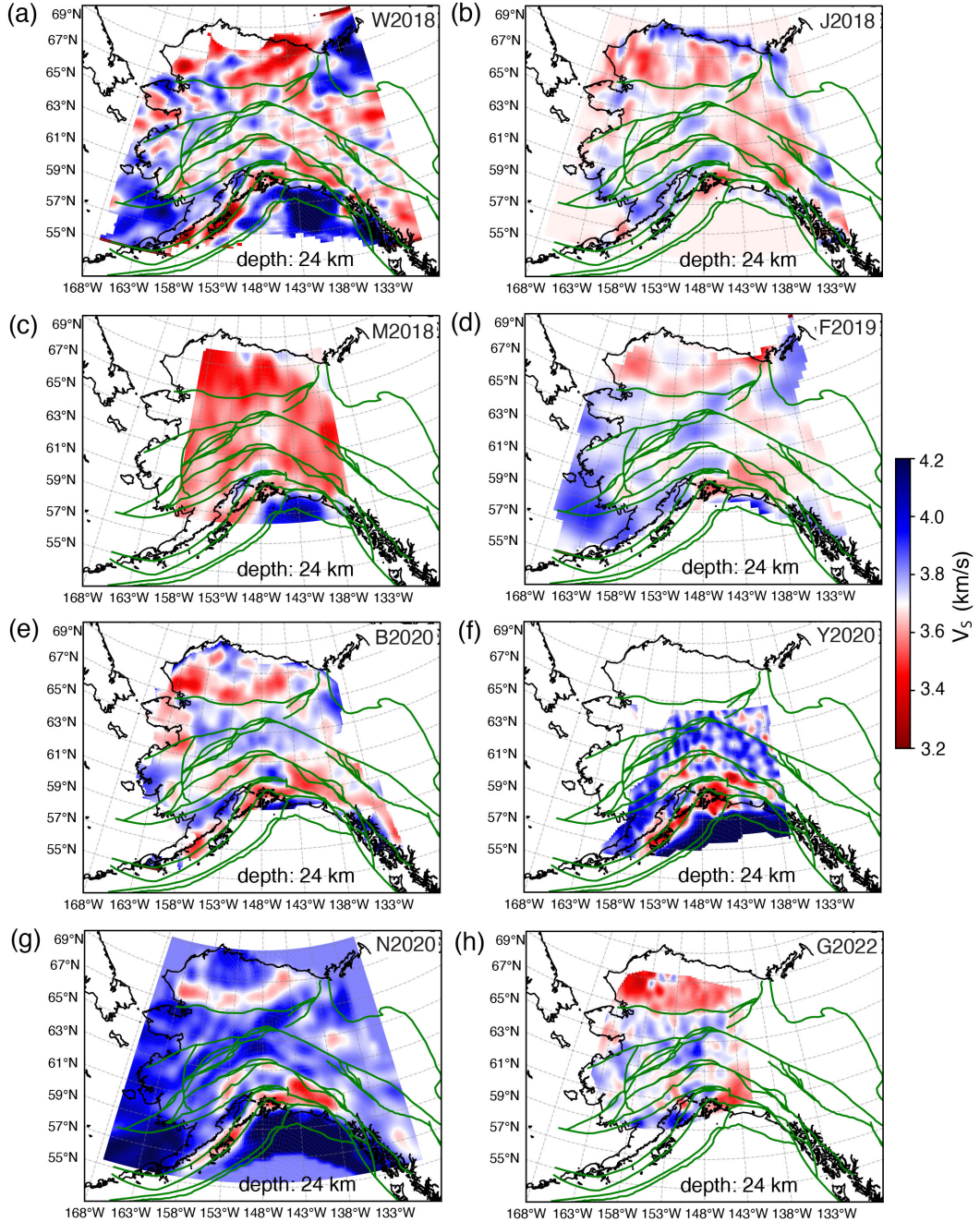


Figure 3. Examples of the synthesized shear-wave velocity models at the depth of 24 km. (a-h) Depth slices from models W2018 (Ward & Lin, 2018), J2018 (Jiang et al., 2018), M2018 (Martin-Short et al., 2018), F2019 (Feng & Ritzwoller, 2019), B2020 (Berg et al., 2020), Y2020 (Yang & Gao, 2020), N2020 (Nayak et al., 2020), and G2022 (Gama et al., 2022b). Major faults (thick green lines) are shown for reference. After interpolations onto 0.2 (longitudes) by 0.1 (latitudes) grids, we smooth all models laterally over five grids for plotting.

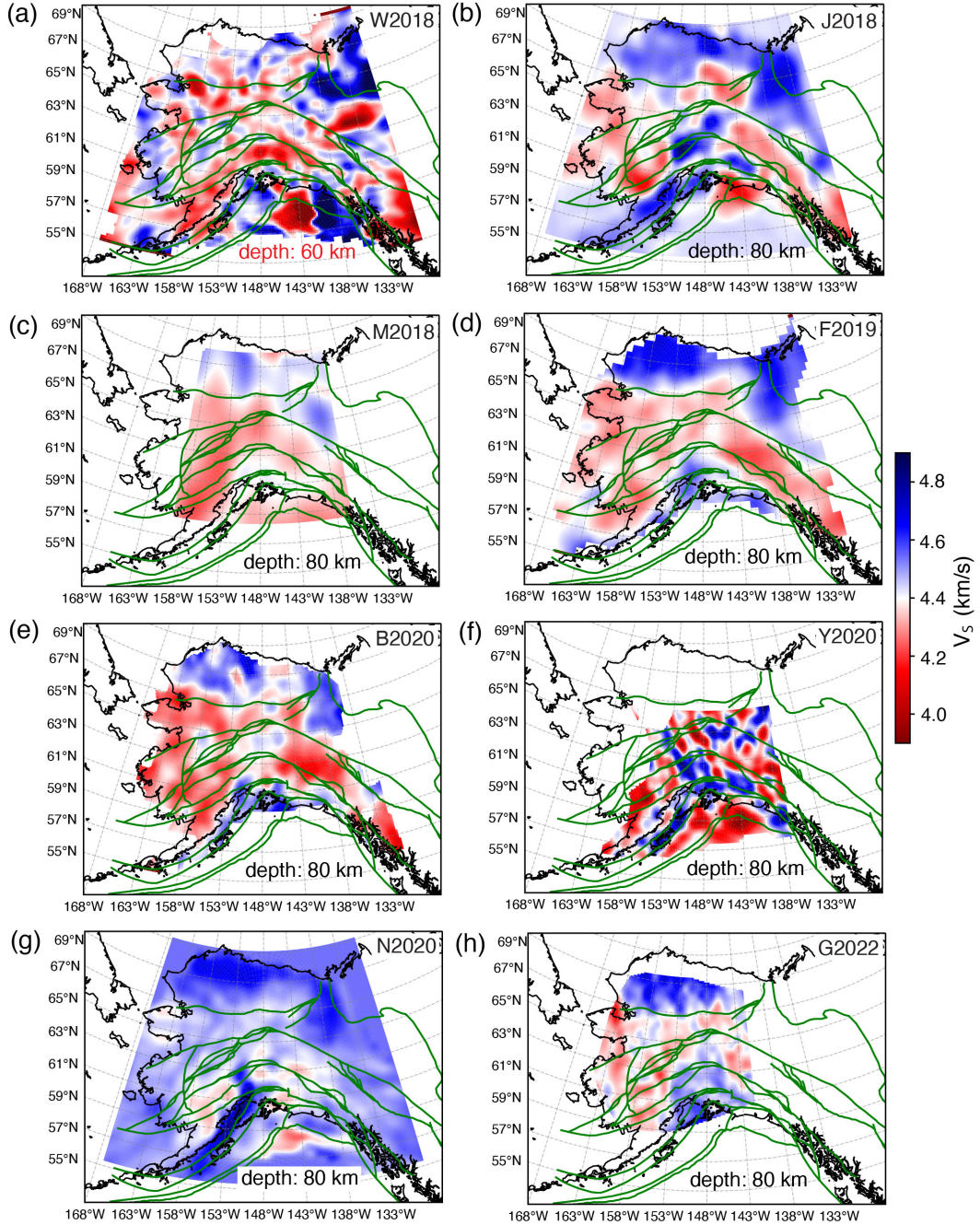


Figure 4. Same as Figure 3 but at the depths of 60 km for W2018 and 80 km for all other models. After interpolating onto 0.2 (longitudes) by 0.1 (latitudes) grids, we smooth all models laterally over five grids for plotting. See Figure S2 in the supplement for the velocity maps at the depth of 60 km for all models.

Table 1. Seismic shear-wave velocity models synthesized in this study (ordered by publication date). For the N2020 model by Nayak et al. (2020), we only consider the AKAN2020 model that covers the entire study area.

Label	Data	Method	Depth (km)	Clusters	Reference
W2018	surface waves from ambient noise and teleseismic P-wave receiver functions	joint inversion	0 to 70	6	Ward and Lin (2018)
J2018	surface waves from ambient noise and teleseismic P-wave arrival times	joint inversion	0 to 800	6	Jiang et al. (2018)
M2018	surface waves from ambient noise and earthquakes and teleseismic P-wave receiver functions	joint inversion	0 to 200	5	Martin-Short et al. (2018)
F2019	surface waves from ambient noise and earthquakes	Bayesian inversion	0 to 200	6	Feng and Ritzwoller (2019)
B2020	surface waves from ambient noise and teleseismic P-wave receiver functions	joint inversion	0 to 144	6	Berg et al. (2020)
Y2020	surface waves from ambient noise	full-wave tomography	0 to 150	5	Yang and Gao (2020)
N2020	surface waves from ambient noise and body waves from earthquakes	travel-time inversion	-1 to 300	6	Nayak et al. (2020)
G2022	surface waves from ambient noise and teleseismic S-wave receiver functions	joint inversion	0 to 226	5	Gama et al. (2022b)

204 Moresi, 2018) (obtained from M. Miller through personal communications) all involve the
 205 analysis of teleseismic P-wave receiver functions, which are time series of converted S waves
 206 generated from passing teleseismic P waves (e.g., Langston, 1977). These studies yield one
 207 value of crustal thickness beneath each seismic station (e.g., Figure 5). The single-station
 208 estimates of crustal thickness based on S-wave receiver functions (e.g., O'Driscoll & Miller,
 209 2015; Gama et al., 2021) are not synthesized in our study because the S-to-P conversion
 210 points lie significantly farther from the station than their P-to-S counterparts. This results
 211 in greater potential inaccuracy when representing crustal thickness with a uniform value.
 212 Additional estimates of crustal thicknesses in Alaska based on P receiver functions also
 213 exist (e.g., Ai et al., 2005; Rondenay et al., 2008, 2010; Kim et al., 2014; Brennan et al.,
 214 2011; Allam et al., 2017), but are not explicitly shown here, mostly because 1) their crustal
 215 thickness values were not digitally available, 2) they did not report crustal thicknesses by
 216 station, or 3) the regions they sample and their specific approaches are similar to one of the
 217 studies in Table 2. Audet et al. (2020) provide robust crustal thickness values from P-wave
 218 receiver functions in western Canada, but the study does not overlap much with our study
 219 area.

Table 2. Crustal thickness models synthesized in this study (ordered by the publication date). Mann et al. (2022) provide two sets of crustal thickness estimates: one for the continental crust beneath southeastern Alaska (Figure 6c), and the other for the thickness of the overriding crust above the subducting slab shallower than the intersection of the top of the slab with the overriding continental Moho (Figure S1 in the supplement, with instructions to access the supplementary information in the **Availability Statement** section). CCP - Common-Conversion-Point stacking, P_S - P-to-S conversions, S_P - S-to-P conversions.

Publication	Single-station estimates	Multi-station estimates	Data	Method
Veenstra et al. (2006)	X	-	P_S	Waveform fitting
Rossi et al. (2006)	X	-	P_S	H- κ stacking
Miller and Moresi (2018)	X	-	P_S	Hand-picked after post-stack migration
Zhang et al. (2019)	X	-	P_S	H- κ stacking
Haney et al. (2020)	-	X	Rayleigh wave phase velocity	Joint inversion for shear-wave velocity and crustal thickness
Mann et al. (2022)	X	X	P_S	2-D post-stack migration and 3-D CCP stacking
Gama et al. (2022a)	-	X	S_P	3-D CCP stacking

The multi-station estimates yield maps of crustal thickness beneath and between nearby stations (e.g., Haney et al., 2020; Gama et al., 2021; Mann et al., 2022), providing overlapping crustal thickness constraints (Figure 6). The crustal thickness maps from both Mann et al. (2022) and Gama et al. (2022a) were generated from back-projecting receiver functions to depth through a velocity model. Mann et al. (2022) used teleseismic P-wave receiver functions, and Gama et al. (2022a) used teleseismic S-wave receiver functions. The map from Haney et al. (2020) was created using an inversion that solves for crustal thickness, as well as the shear velocity of the crust and an underlying mantle half-space, with an approximation based on the Dix equation to relate fundamental mode Rayleigh wave phase velocities to the velocity model. The criteria used in selecting these studies are: 1) they provide semi-continuous estimates of crustal thickness that were digitally available, and 2) they employed EarthScope Transportable Array data.

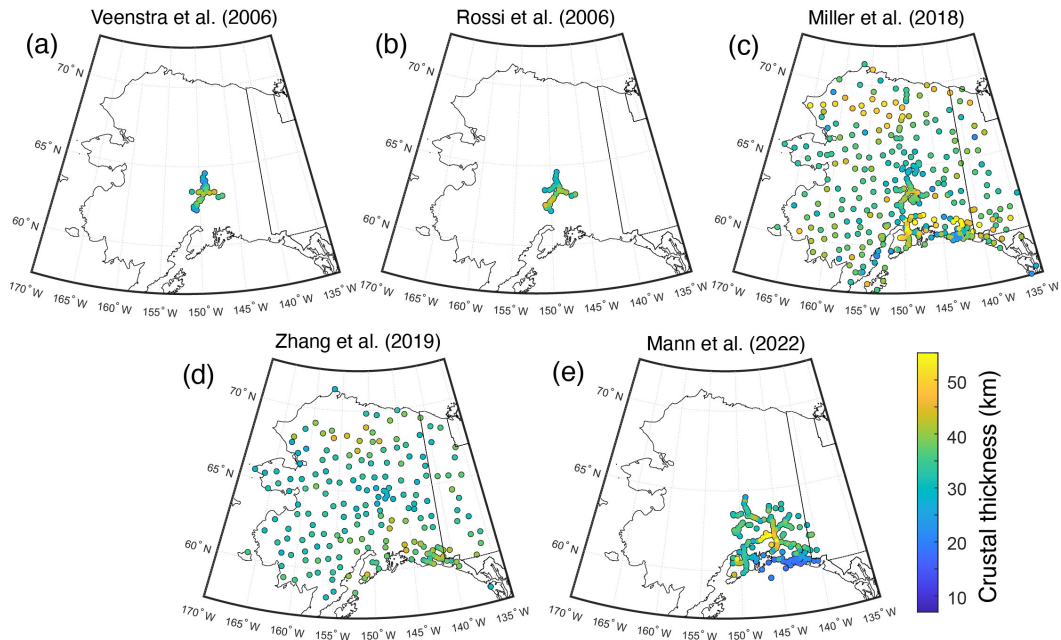


Figure 5. Single-station crustal thickness estimates from (a) Veenstra et al. (2006), (b) Rossi et al. (2006), (c) Miller and Moresi (2018), (d) Zhang et al. (2019), and (e) Mann et al. (2022).

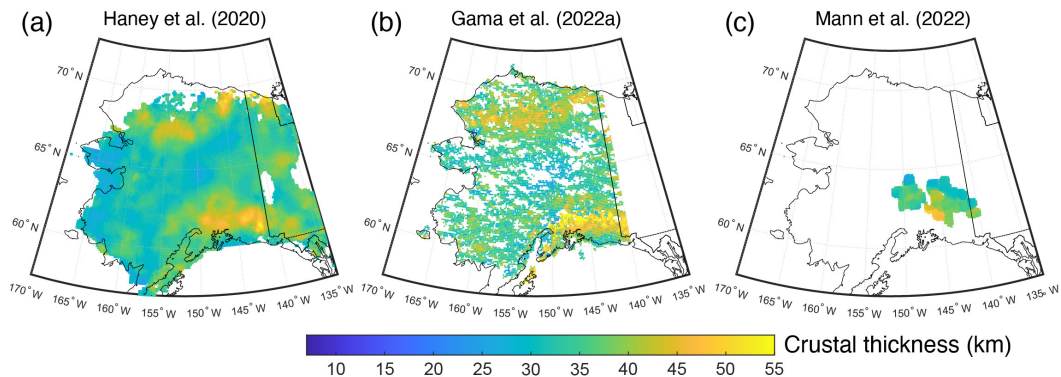


Figure 6. Multi-station continental crustal thickness estimates from (a) Haney et al. (2020), (b) Gama et al. (2022a), and (c) Mann et al. (2022).

In addition to the seven studies selected for this synthesis study, other approaches to measuring crustal thickness have also been applied in Alaska. Among studies that solve for 3D velocity structure, those that jointly invert surface wave dispersion with P receiver functions (e.g., Martin-Short et al., 2018; Ward & Lin, 2018; Feng & Ritzwoller, 2019; Berg et al., 2020) or with S receiver functions (e.g., Gama et al., 2021, 2022b) typically provide sharper resolution of the depth of the Moho velocity gradient than other approaches. However, the studies in these groups that sample mainland Alaska are represented in the analysis of shear-wave velocity models in Section 2.1, and their crustal thickness results are not explicitly considered in this section.

Among the selected studies (Table 2), the estimation of crustal thickness becomes complex in the southern part of the subduction zone, where the subducting crust is in contact with the overriding crust. In this case, there are typically multiple sharp velocity gradients as a function of depth (e.g., Bostock, 2013), including the Moho of the subducting plate, the base of the crust of the upper plate, and the interface between the two plates. Mann et al. (2022) mapped out the depth of the plate interface at depths <60 km (Figure S1 in the supplement, which is available through the Zenodo repository as described in **Availability Statement**). To approximately delineate the northern edge of the area where the Moho of the subducting plate is stacked beneath the crust of the upper plate, we use the plate interface depths of Mann et al. (2022) to determine the location of a line, referred to as the Plate Interface Extent (PIE) line. This hypothetical line represents where the top of the slab intersects the base of the continental crust. For simplicity, we assume that this contact occurs at a depth of 40 km (Figure S1 in the supplement), which is a reasonable approximation based on higher resolution velocity gradient profiles along lines of denser stations Mann et al. (2022). In reality, the depth at which the top of the slab is in contact with the upper plate Moho varies, but accurately capturing this variation along the complete PIE line exceeds the resolution of existing studies. However, the 40 km contact depth is sufficient for our purposes, since the goal of the PIE line is simply to approximate where the continental crust is in contact with the subducting plate and multiple velocity gradients exist that obscure crustal thickness estimates. Mann et al. (2022) directly accounted for the multiple crustal velocity gradients when measuring the plate interface depth, which is equivalent to the thickness of the overriding continental crust south of the PIE line (Figure S1 in the supplement).

Note, although we use the term plate interface extent (PIE), we emphasize that it is intended as a crust-crust contact in that it refers to the separation of the top of the crust of the downgoing plate from the base of the crust in the overriding plate. If there is any mantle lithosphere present in the overriding plate, then the top of subducting crust would be in contact with the mantle lithosphere at the base of the overriding plate north of the PIE line.

3 Methods

To synthesize the two different types of models, i.e., the shear-wave velocity models and the crustal thickness models, we apply two categories of analyses. Considering lateral variations in the shear-wave velocity models, we use unsupervised K-means clustering of the 1-D velocity profiles to objectively analyze the regionalization of the 3-D velocity structure. This is also a way to reduce the dimension of the velocity models for the synthesis and has been effective in tectonic regionalization of global seismic velocity models (e.g., Lekic & Romanowicz, 2011; Schaeffer & Lebedev, 2015; Eymold & Jordan, 2019). For the crustal thickness models, we focus on the statistical analysis of all models by averaging the crustal thickness estimates. In the following paragraphs, we describe the details of the procedures for comparing and synthesizing the selected seismic models.

281 **3.1 K-means clustering of 1-D seismic velocity profiles**

282 K-means clustering is commonly used to group data points based on their distances
 283 from the cluster centers. We use the *Tslearn* Python toolkit (Tavenard et al., 2020) for
 284 K-means clustering of time-series data to cluster the seismic velocity profiles (1-D depth
 285 profiles). The clustering operations are implemented as Python wrapper functions in the
 286 *SeisGo* toolbox (Yang et al., 2022a, 2022b). As described in Section 2.1, all velocity models
 287 are resampled onto the same 3-D grid with spacings of 0.2° in the longitudinal direction,
 288 0.1° in the latitudinal direction, and 2 km in the depth direction. The resampled velocity
 289 models are clustered through the following steps (see Section 4.1 for the description of key
 290 observations):

291 *Step 1: Determine the depth range for clustering.* The velocity models to be analyzed
 292 have different depth ranges. This step sets the depth range of interest. From Figures 3 and 4
 293 and Section 2.1, we observe varying velocity patterns from different velocity models, though
 294 they all show a lateral variation of velocities across Alaska and western Yukon (Canada).
 295 However, Figure 3 (as an example of crustal velocities) and Figure 4 (as an example of
 296 mantle lithosphere velocities) reveal different velocity features. Therefore, in this study, we
 297 divide the continental lithosphere into two depth ranges: 10-50 km and 40-120 km. We use
 298 the minimum depth of 10 km to account for the lack of resolution at shallower depths in
 299 some of the velocity models, such as J2018 (Jiang et al., 2018), M2018 (Martin-Short et
 300 al., 2018), and Y2020 (Yang & Gao, 2020). Considering the overall crustal thickness within
 301 the study area (Section 2.2 and Figures 5 and 6), we use the depth range of 10-50 km to
 302 represent the crust for clustering purposes. The depth of 120 km would include the total
 303 thickness of the upper plate lithosphere over most of the study area, with the exception of
 304 some of the thickest lithosphere in northern Alaska (Miller et al., 2018; Gama et al., 2021,
 305 2022b). However, in central Alaska, the lithosphere is much thinner (Gama et al., 2022a),
 306 and a maximum depth of 120 km would also include the asthenospheric mantle. Hence we
 307 use the depth range of 40-120 km for the mantle clustering analysis, to capture variations
 308 in the structure of the mantle lithosphere of the continental plate while avoiding too much
 309 dilution of the lithospheric structure by the asthenospheric mantle.

310 *Step 2: Choose the number of clusters for each velocity model.* Specifying the number
 311 of clusters is required to run K-means clustering. To account for the different coverage of
 312 each velocity model, we choose 6 clusters for models that cover all of Alaska and the western
 313 Yukon (Canada) area, including W2018, J2018, F2019, B2020, and N2020 models (Figure
 314 2b and Table 1). For models that only cover portions of the study area, including M2018,
 315 Y2020, and G2022, we choose 5 clusters (Figure 2b and Table 1). The clustering function in
 316 *SeisGo* (Yang et al., 2022a) has the option of automatically determining the optimal number
 317 of clusters. For models in Table 1, the automatically determined numbers of clusters range
 318 from 5 to 8, resulting in small-scale clusters in some cases while producing similar major
 319 clusters as the results that use the pre-assigned number of clusters. Although the choice of
 320 the number of clusters is somewhat subjective, it does not change the overall conclusions of
 321 the analysis (Section 4).

322 *Step 3: Smooth the 3-D velocity model and build an ensemble of 1-D velocity profiles.*
 323 Due to the difference in data and methods, the selected velocity models may have different
 324 spatial resolutions. For instance, models W2018 (Ward & Lin, 2018) and Y2020 (Yang &
 325 Gao, 2020) show more small-scale features than other models (Figures 3 and 4). To focus on
 326 major velocity clustering patterns, we smooth all velocity models with a boxcar smoother
 327 across 5 grid points in both longitudinal and latitudinal directions but not in the depth
 328 direction. After smoothing the model, we build an ensemble of 1-D velocity profiles. The
 329 1-D velocity profile at each longitude-latitude grid can be treated as a time series. This step
 330 generalizes the seismic velocity clustering into the clustering of a time series dataset.

331 *Step 4: Conduct clustering of the ensemble of 1-D velocity profiles.* We use the Eu-
 332 clidean distance as the distance metric in clustering. The clustering results are shown in

333 Figures 7 and 8 for the depths of 10-50 km and 40-120 km, respectively. The cluster labels
 334 are randomly assigned for each velocity model and are not directly comparable across dif-
 335 ferent models. The cluster centers and the standard deviations are shown in Figures S3 and
 336 S4 for the depths of 10-50 km and 40-120 km, respectively.

337 *Step 5: Detect cluster boundaries.* To compare the regionalization of the velocity struc-
 338 tures from different models, we detect the boundaries between clusters from the clustering
 339 images that are color-coded by the cluster labels (Figures 7 and 8). We compute the binary
 340 gradient around each resampled model grid or image pixel. The gradient is 0 if all four
 341 pixels have the same cluster label as the center pixel and 1 if there is at least one neighbor-
 342 ing pixel in a different cluster, which means the center pixel is at a cluster boundary. The
 343 detected cluster boundaries for each velocity model are shown as red pixels in Figures S5
 344 and S6 in the supplement for the clustering results at the depth of 10-50 km and 40-120 km,
 345 respectively.

346 *Step 6: Compute votes of cluster boundaries from all models.* To highlight the cluster
 347 boundaries that are shared by multiple velocity models, we stack all images of the cluster
 348 boundaries and compute the total times a model grid (or image pixel) is detected as a cluster
 349 boundary. This step produces a vote map showing the distribution of cluster boundaries
 350 with all velocity models (Figure 9a-b). A higher vote means more models detect the cluster
 351 boundaries. From the vote maps of detected cluster boundaries, we identify the major
 352 velocity domains as outlined by cluster boundaries with ≥ 3 votes and extract the average
 353 velocity profiles within the domains (Figure 10). To minimize the bias, we pick cluster
 354 boundary lineaments and velocity domains solely based on the cluster boundary vote maps
 355 without referencing the fault lines and tectonic terranes.

356 3.2 Averaging of crustal thickness estimates

357 We compute the average and standard deviation of crustal thicknesses separately for
 358 the compiled single- and multi-station results (Table 2). For each, we determine values
 359 that fall within grid nodes spaced 0.5° (longitude) by 0.25° (latitude) apart (Figure 11
 360 and S9 in the supplement). The choice of grid spacing is based on the typical station
 361 spacing in the study area (50-80 km). We adopt a two-step averaging approach including
 362 taking the mean of values from a given study within the grid element and then taking
 363 the mean and standard deviation of the mean values from each study. This approach
 364 equalizes the influence of a given study within a grid element. For the multi-station crustal
 365 thickness map (Figure 11b), we use the plate interface depth from Mann et al. (2022)
 366 (Figure S1 in the supplement) as the thickness of the overriding continental crust south of
 367 the PIE line, avoiding complexity due to the presence of both the upper-plate crust and
 368 the subducting crust. North of the PIE line, the crustal thickness simply corresponds to
 369 the mean Moho depth estimate, which is the base of the continental crust. When averaging
 370 crustal thicknesses, uncertainties in individual values are not taken into account, in part
 371 because not all studies report uncertainties. However, to estimate the potential impact of
 372 uncertainties in the input data, we also calculate the map of multi-station crustal thickness
 373 using uncertainties for each data point from the contributing studies as inverse weights
 374 at both stages of averaging. Gama et al. (2022a) provided a standard deviation for each
 375 crustal thickness value. Haney et al. (2020) estimated an uncertainty of 3.5 km for their
 376 crustal thicknesses, and an uncertainty of 3.0 km was estimated from the crustal thicknesses
 377 by Mann et al. (2022). Overall, these uncertainties place more weight on the values from
 378 Haney et al. (2020) and Mann et al. (2022). However, the resulting map of mean crustal
 379 thicknesses (Figure S10a in the supplementary information) is very similar to the result
 380 without considering uncertainties (Figure 11b), and the differences are typically less than 1
 381 km (Figure S10b in the supplementary information).

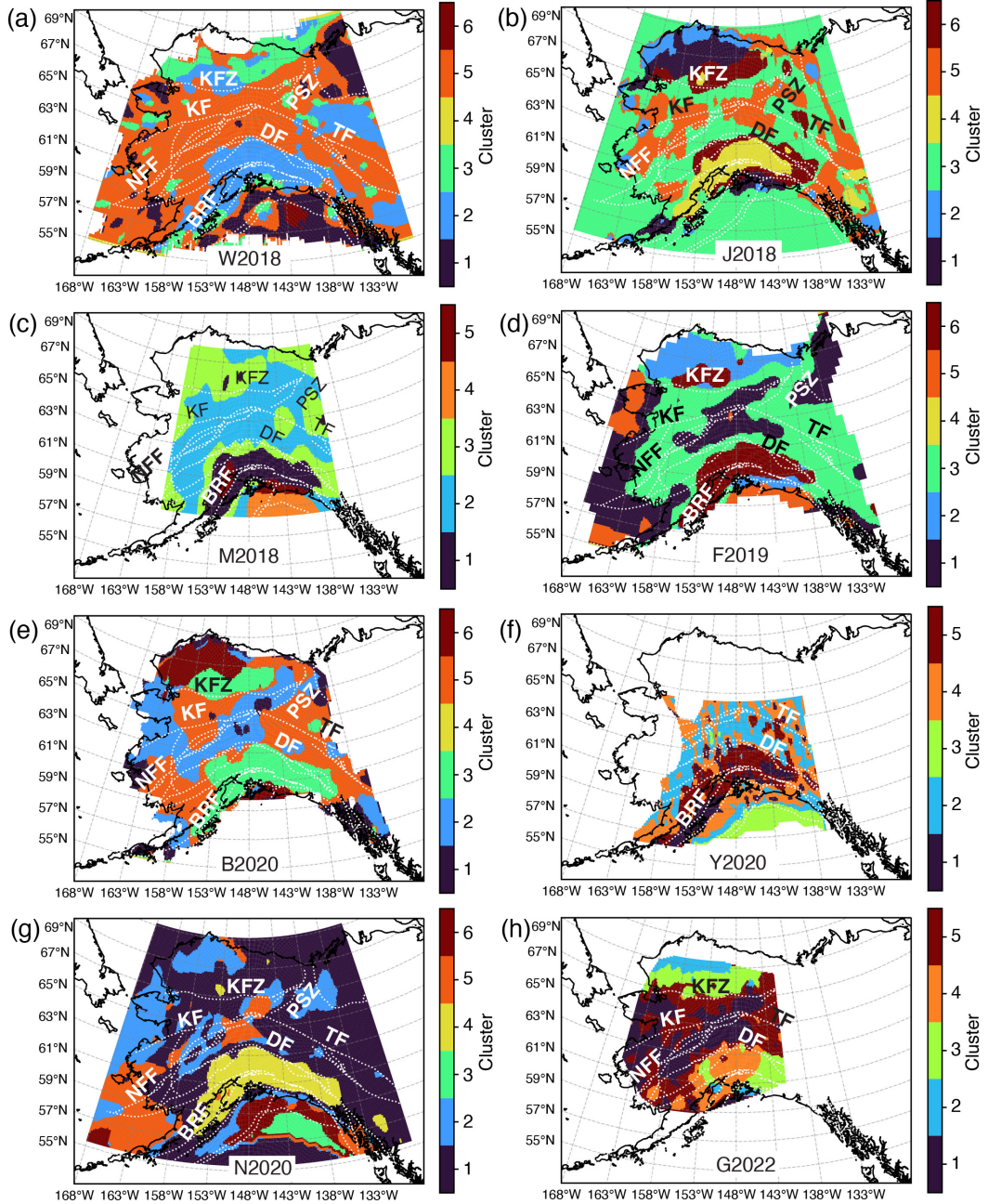


Figure 7. Clustering of velocity profiles between 10-50 km depths. The randomly-assigned cluster numbers are color-coded for each velocity model. The same cluster numbers for different velocity models may correspond to different velocity profiles. (a-h) Clustering results for models W2018 (Ward & Lin, 2018), J2018 (Jiang et al., 2018), M2018 (Martin-Short et al., 2018), F2019 (Feng & Ritzwoller, 2019), B2020 (Berg et al., 2020), Y2020 (Yang & Gao, 2020), N2020 (Nayak et al., 2020), and G2022 (Gama et al., 2022b). The dotted white lines are the fault lines as in Figure 1b. Labels of major faults: KFZ - Kobuk Fault Zone, KF - Kaltag Fault, PSZ - Porcupine Shear Zone, NFF - Nixon Fork-Iditarod Fault, TF - Tintina Fault, DF - Denali Fault System, BRF - Border Range Fault.

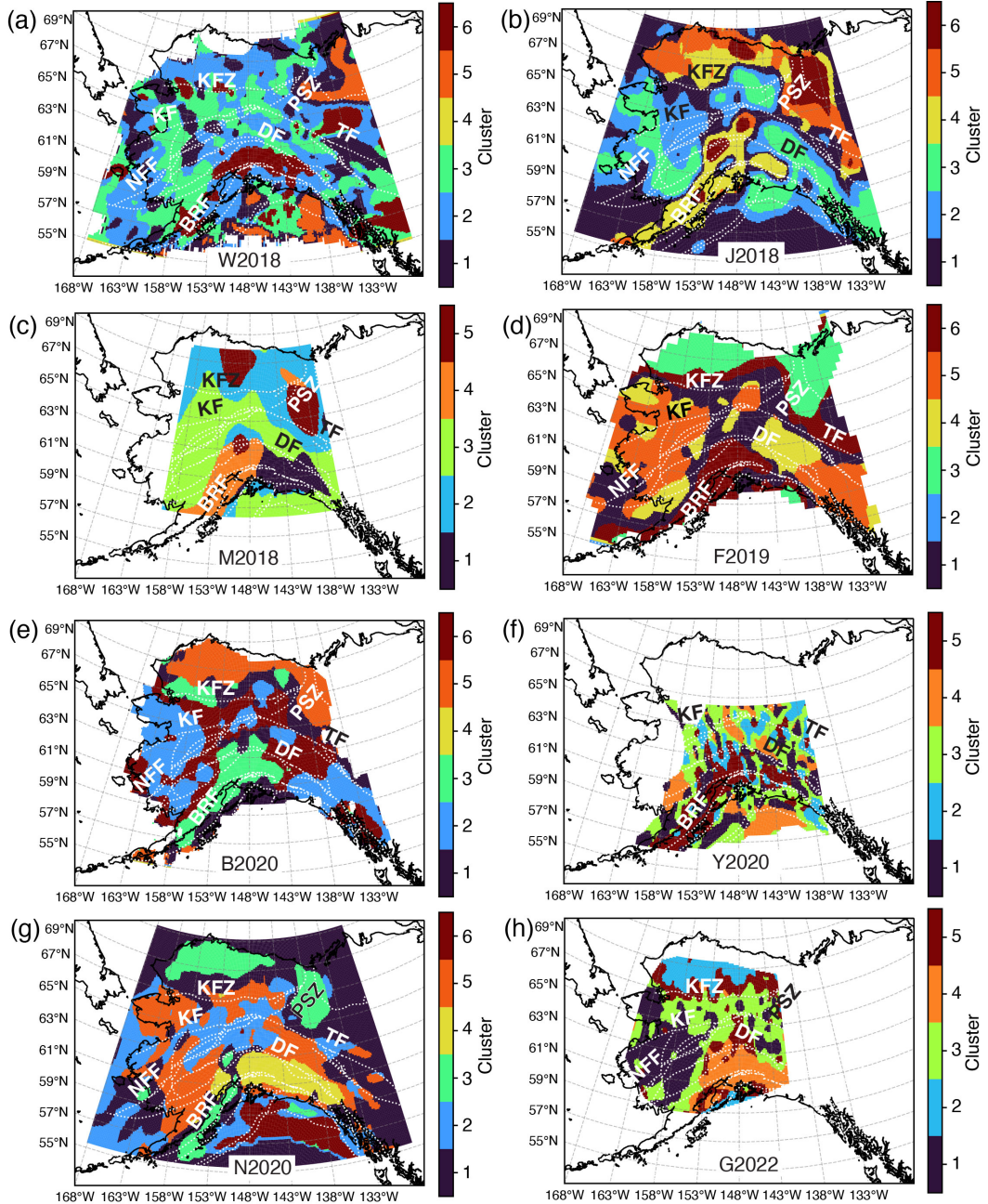


Figure 8. Same as Figure 7 but for velocity profiles at the depths of 40-120 km. The randomly-assigned cluster numbers are color-coded for each velocity model. The dotted white lines are the fault lines as in Figure 1b. See Figure 7 for the labels of major faults.

382 **4 Results**383 **4.1 Cluster maps of seismic velocity profiles**

384 The clustering of crustal velocities (10-50 km) highlights the lateral variations correlated
 385 with major faults (Figure 7). In the cluster map of model W2018 (Figure 7a), the southern
 386 Alaska region south of the Denali Fault System is dominated by cluster 2. The region north
 387 of the Kobuk Fault Zone shows three clusters (2, 3, and 5). The western Yukon region is
 388 characterized by clusters 1, 2, and 5. The rest of the study area, mostly between the Kobuk
 389 Fault Zone and the Denali Fault System, is characterized by cluster 5. The clustering
 390 patterns from south to north across Alaska separated by the Denali Fault System and the
 391 Kobuk Fault Zone can also be observed from other models (Figure 7b-7e and 7g-7h). The
 392 cluster map of Y2020 (Figure 7f) also reveals the contrast in velocity patterns across the
 393 Denali Fault System, although lacks coverage in northern Alaska. Models J2018, F2019,
 394 B2020, N2020, and G2022 also show the variation of velocity patterns/clusters from west
 395 to east across Alaska, as well as across the Porcupine Shear Zone in northeastern Alaska
 396 (Figure 7d, 7e, and 7g-7h). In addition, the Pacific Plate in the northern Gulf of Alaska is
 397 characterized as separated clusters in models W2018 (clusters 1 and 6), M2018 (cluster 4),
 398 F2019 (cluster 5), Y2020 (cluster 3), and N2020 (clusters 3 and 6) with prominently higher
 399 velocities than the onshore area (Figure S3 in the supplement).

400 The velocity clustering patterns in the mantle lithosphere (40-120 km) show correlations
 401 with both major faults and the subduction zone along the southern margin of Alaska
 402 (Figure 8). We observe separated clusters across the Kobuk Fault Zone (models W2018,
 403 J2018, F2019, B2020, N2020, and G2022 in Figure 8a-b, d-e, and g-h), the Porcupine Shear
 404 Zone (models W2018, J2018, M2018, F2019, B2020, and N2020 in Figure 8a-e and g), the
 405 Kaltag Fault (model N2020 in Figure 8g), the Denali Fault System from all models, and
 406 the Tintina Fault (models W2018, J2018, M2018, F2019, B2020, and N2020 in Figure 8a-e
 407 and g). However, some of the cluster boundaries only follow part of the fault lines. In
 408 southwestern Alaska, we observe elongated cluster regions sub-parallel to the subduction
 409 margin in multiple cluster maps, including the results from models J2018 (cluster 4), M2018
 410 (cluster 4), F2019 (clusters 4 and 6), B2020 (cluster 3), Y2020 (cluster 5), N2020 (clus-
 411 ters 3 and 5), and G2022 (cluster 3). Most of these margin-parallel zones are located west
 412 of approximately 150°W in longitude. To the east, some models reveal a different cluster
 413 parallel to the margin, such as cluster 3 in J2018, cluster 1 in M2018, cluster 2 in B2020,
 414 cluster 4 in N2020, and cluster 4 in G2022. In Y2020, cluster 5 spans across the majority
 415 of the margin with a gap at around 145°W in longitude (Figure 8f). It is worth noting that
 416 parts of these margin-parallel cluster zones overlap with the crustal clusters to the south
 417 of the Denali Fault System (Figure 8d-e and g-h). Compared to the crustal cluster maps
 418 in Figure 7, the mantle cluster maps contain more small-scale variability, particularly those
 419 from models W2018 (Figure 8a), J2018 (Figure 8b), and G2022 (Figure 8h).

420 **4.2 Major velocity domains revealed by cluster boundaries**

421 The vote maps of the velocity model cluster boundaries reveal major structural domains
 422 shared across multiple velocity models. The cluster boundaries from individual models show
 423 different patterns from model to model (Figures S5-S6 in the supplement). However, by
 424 combining the detection of cluster boundaries from all models, the vote maps in Figure 9
 425 highlight the cluster boundaries that are shared by multiple velocity models, shown as darker
 426 colors. Figure 10 shows the cluster boundary vote maps (blue pixels) with ≥ 3 votes. Due
 427 to the difference in spatial coverage of different models (Figure 2b), southern and central
 428 Alaska are sampled by all eight models, while other areas are sampled by at least five models.
 429 The threshold of 3 strikes a balance between highlighting major velocity domains shared by
 430 multiple models and having enough connectivity among pixels of the cluster boundaries to
 431 show major lineaments.

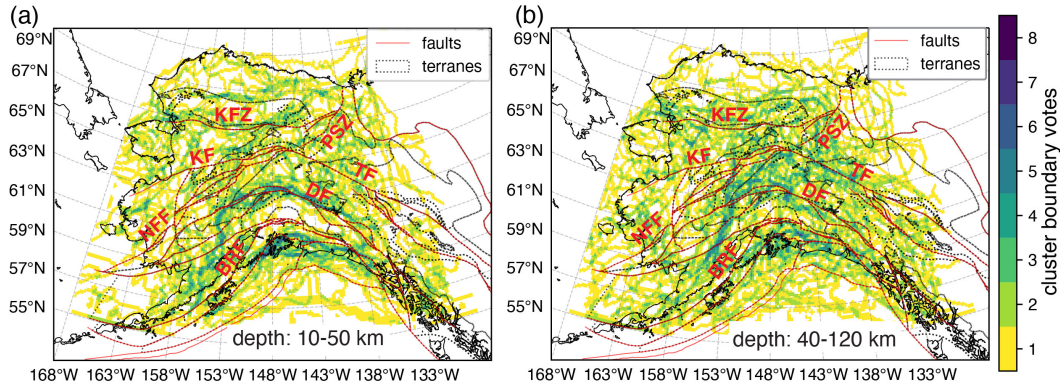


Figure 9. Detected cluster boundaries from all velocity models. (a-b) Cluster edge vote counts for the depths of 10-50 km and 40-120 km, respectively. Major faults (red solid lines) and terrane outlines (gray dotted lines) are shown for reference. See Figure 7 for the labels of major faults.

We identify 6 major velocity domains in the crust (C1-C6) and mantle lithosphere (M1-M6) defined by the cluster boundary lineaments (Figure 10a-b). These velocity domains outline major areas without noticeable lineaments of cluster boundary votes. Domain C1 overlaps with most of the area north of the Brooks Range in northern Alaska. C2 is mostly along the Brooks Range. Domains C3-C5 are located in the interior and western Alaska between the Brooks Range to the north and the Alaska Range to the south. C6 is located in southern Alaska covering the Alaska Range and the region to the south. For the mantle lithosphere, domain M1 spans across the Brooks Range and the North Slope area to the north. M2 occupies most of western Alaska and part of the interior. M3 is located to the southeast of M1 and to the east of M2. To the south, it is adjacent to domain M4, which is characterized by a group of small-scale cluster boundaries. To the south of M4, domains M5 and M6 are separated by a northwest-southeast trending cluster boundary lineament approximately along the Denali Fault System.

4.3 Velocity profiles within major domains

The average velocity profiles within the crustal velocity domains show similar overall patterns of increasing velocities with depth (Figure 10c). The velocities within domain C1 are lower than those within domains C3-C5 at the depths of <25 km. The velocities within domain C6 are lower than those for C3-C5 below the depth of 25 km. Domain C2 has velocities that are typically 0.2-0.3 km/s lower than other domains. The average shear-wave velocities reach 4.2 km/s at the depth of 35 ± 2 km within domains C1 and C3-C5, 40 ± 1 km within domain C2, and 45-46 km within domain C6. Domain C6 south of the Denali Fault System indicates the smallest velocity change over the entire depth range from 3.5 km/s to 4.25 km/s. In contrast, domain C1 shows the largest velocity range from 3.25 km/s to 4.5 km/s. However, there are notable variations across different velocity models for these domains (Figure S7 in the supplement).

The mantle velocity domains show distinctly different average velocity profiles, particularly below the depth of 45 km (Figure 10d). Domain M1 has the overall highest velocity of 4.5-4.6 km/s below the depth of 50 km. Domains M2 and M6 both show a low-velocity zone at depths of about 60-120 km with a minimum velocity of 4.3 km/s at the depth of about 100 km. Domain M3 also contains a decrease in velocity at a similar depth range as M2 and M6 but with a lower amplitude. Below the depth of 45 km, domain M4 has the smallest overall velocity variation with an almost constant velocity of 4.4 km/s. Domain M5 shows the largest velocity variation of 0.5 km/s from 4 km/s to 4.5 km/s. The velocity profile for

465 domain M5 is also monotonically increasing, although the rate of increase becomes small
 466 below the depth of 90 km. Similar to the crustal domains, while we focus more on the
 467 average profiles, it is worth noting that the velocity profiles for the mantle domains also
 468 vary significantly across different models (Figure S8 in the supplement).

469 4.4 Average crustal thickness

470 The average crustal thicknesses are shown in Figure 11a for the single-station averages
 471 and in Figure 11b for the multi-station averages north of the PIE line. The standard
 472 deviations in the single station estimates are much higher south of the PIE line than to
 473 its north (Figure S9b), reflecting larger discrepancies among different studies in this region.

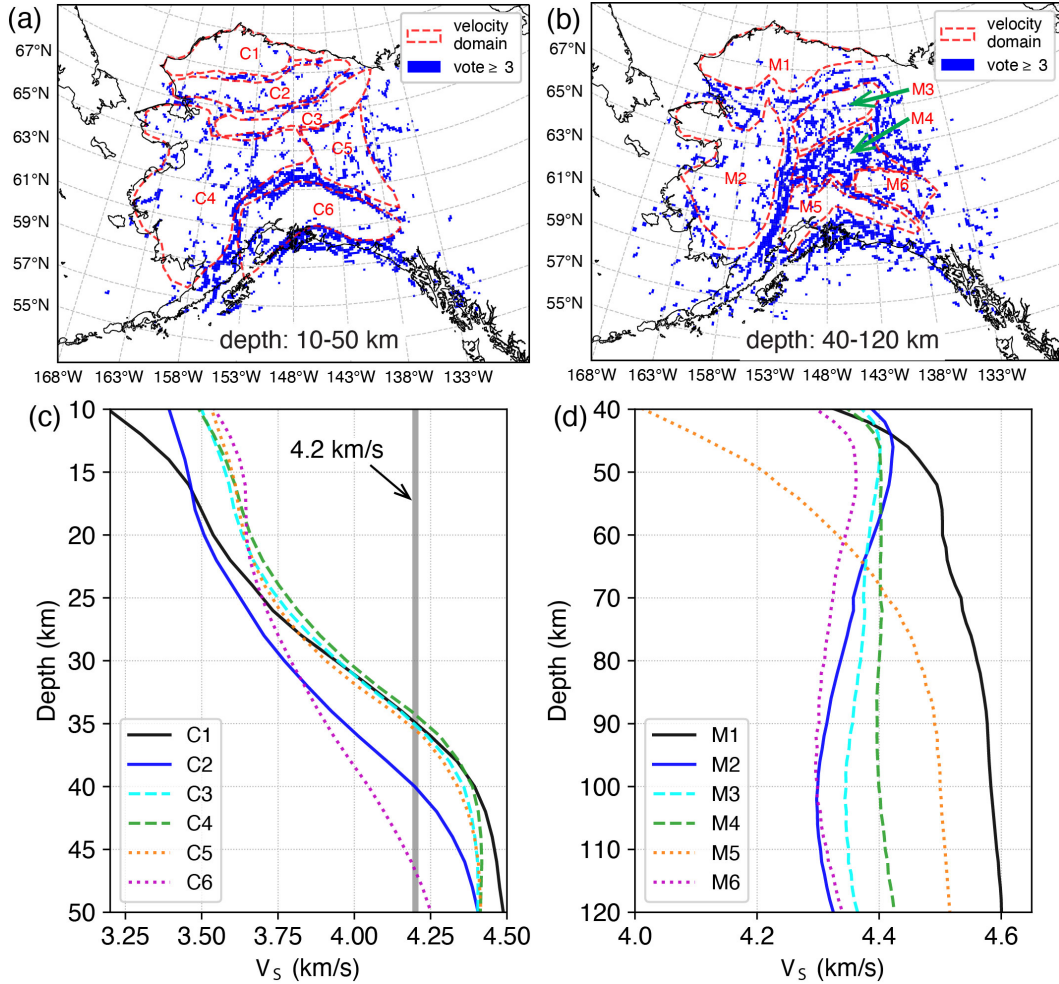


Figure 10. Major seismic velocity domains and the average velocity profiles. (a-b) Identified major velocity domains (alphanumeric labels C1-C6 and M1-M6 within the red dashed outlines) with ≥ 3 votes (blue pixels) for the depths of (a) 10-50 km and (b) 40-120 km. (c-d) Velocity profiles within each velocity domain averaged across all models at the depths of (c) 10-50 km and (d) 40-120 km. The thick gray vertical line in (c) is the $V_S=4.2$ km/s line as the minimum velocity of melt-free ultramafic materials (e.g., Delph et al., 2021), which is used here as a proxy to denote the velocity at the bottom of the crust. See Figures S7-S8 in the supplement for the velocity profiles from different velocity models for each velocity domain.

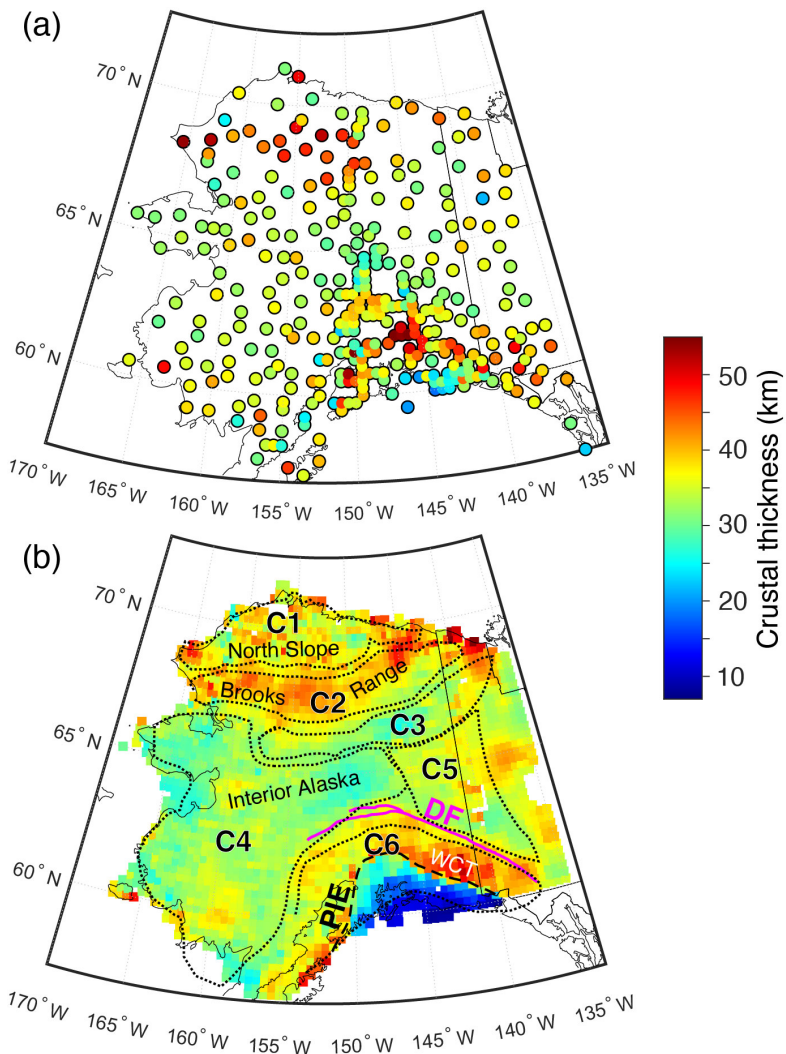


Figure 11. Average crustal thicknesses from multiple models. (a) Average of crustal thicknesses for single-station estimates. (b) Average of multi-station crustal thicknesses within each 0.5° (longitude) by 0.25° (latitude) bin. The dotted lines are outlines of the crustal seismic velocity domains as in Figure 10a, defined based on velocity clustering results. To the south of the Plate Interface Extent (PIE) line, the map is showing the depth to the top of the subducting plate. DF - Denali Fault System, WCT - Wrangellia Composite Terrane.

This may result from the presence of multiple positive velocity gradients within both the upper plate and the shallowly-dipping downgoing plate in this region, which includes the Yakutat crust. For example, different studies may have selected different positive velocity gradients below a given station as the Moho, resulting in discrepancies in inferred crustal thicknesses. South of the PIE line in the mean crustal thickness map from the multi-station estimates (Figure 11b), the upper plate crustal thickness is represented by the plate interface depth. North of the PIE line, the multi-station crustal thicknesses (Figure 11b) show a good agreement overall with the average of the single-station estimates (Figure 11a). However, in some locations, the average crustal thicknesses differ by more than 15 km. Some of these discrepancies are significant, in the sense that the standard deviations for the mean crustal thicknesses do not overlap. The Moho depth standard deviations north of the PIE line are typically lower for the multi-station crustal models (Figure S9d) than for the single-station results (Figure S9b), indicating more consistency across the individual multi-station crustal thickness models. Given this greater consistency and the more continuous lateral coverage provided by the multi-station models, we recommend the crustal thicknesses in Figure 11b as a reference model for continental Alaska.

We observe four notable crustal thickness patterns as revealed by the preferred reference model for Alaska (Figure 11b). 1) The crust across much of interior Alaska, approximately between the Alaska Range to the south and the Brooks Range to the north, is about 25–35 km thick, similar to the observations from previous studies (e.g., Woppard et al., 1960; Clarke & Silver, 1991; Searcy et al., 1996; Ai et al., 2005; Rossi et al., 2006; Veenstra et al., 2006; Brennan et al., 2011; Allam et al., 2017; Miller et al., 2018; Martin-Short et al., 2018; Zhang et al., 2019; Haney et al., 2020; Gama et al., 2021, 2022a, 2022b; Mann et al., 2022). 2) The Brooks Range in northern Alaska has a 40–50 km thick crust, which is similar to previous estimates (e.g., Woppard et al., 1960; Fuis et al., 1995, 1997; Searcy et al., 1996; Miller et al., 2018; Zhang et al., 2019; Haney et al., 2020; Gama et al., 2021, 2022b, 2022a). 3) The Wrangellia composite terrane in the south has a 35–55 km thick crust, as in previous studies (e.g., Fuis & Plafker, 1991; Haney et al., 2020; Gama et al., 2022a, 2022b). The crustal thickness of the Wrangellia composite terrane south of the Denali Fault System increases from 35 km to >50 km from west to east. 4) A laterally sharp northward decrease in crustal thickness of about 10 km exists across the Denali Fault System, similar to the observations in previous studies (e.g., Rossi et al., 2006; Veenstra et al., 2006; Brennan et al., 2011; Ward & Lin, 2018; Allam et al., 2017; Miller et al., 2018; Martin-Short et al., 2018; Haney et al., 2020; Mann et al., 2022; Gama et al., 2022a, 2022b). This change in crustal thickness is most laterally localized at the Denali Fault System between 140°W and 146°W. In the central segment of the Denali Fault System (at 146°W to 150°W) the decrease in crustal thickness is distributed across both the Denali and Hines Creek faults. Further to the west, the northward decrease in crustal thickness becomes lower amplitude and/or more gradual and is less clearly associated with the Denali fault trace.

5 Discussion

The patterns highlighted in Section 4 reveal major domains in terms of the integrated shear-wave velocity models (Figures 9 and 10) and crustal thicknesses (Figure 11). In this section, we place these results in the context of Alaskan tectonics and the evolution of the continental lithosphere.

5.1 Influence of crustal thickness on velocity clustering

The crustal velocity domains defined by the clustering of velocity profiles demonstrate a strong correlation with the crustal thickness patterns (Figure 11b). To examine the quantitative relationship between crustal thickness patterns and the velocity domains, we extract the average crustal thickness in each domain for both the crustal and mantle velocity domains (Figure 12). We also compare the crustal thickness within the crustal velocity

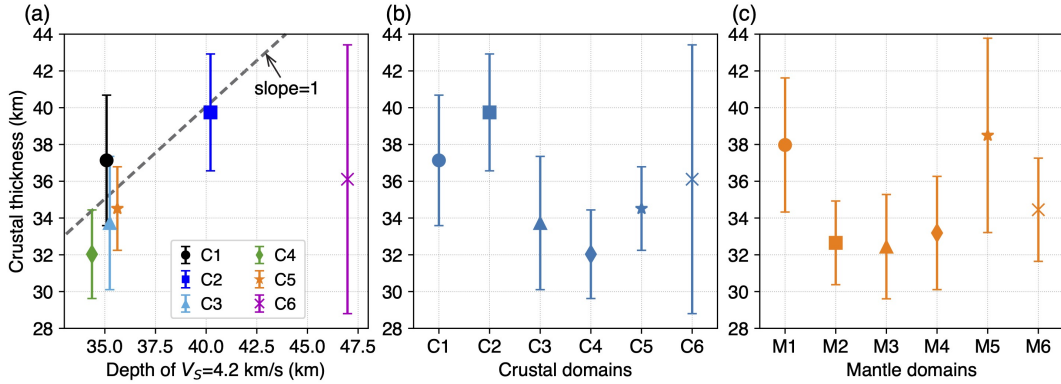


Figure 12. Crustal thicknesses within the crustal (C1-C6) and mantle (M1-M6) velocity domains using the multi-station average model in Figure 11b. (a) Comparison of crustal thicknesses within the crustal velocity domains (C1-C6) and the depths to the $V_S=4.2$ km/s on the average velocity profiles in Figure 10c. The error bar shows the standard deviation of the crustal thicknesses within each domain. The dashed line, with a slope of 1, is plotted for reference. (b) Crustal thicknesses within the crustal velocity domains (C1-C6) as defined by clustering of the velocities at the depths of 10-50 km. (c) Crustal thicknesses within the mantle velocity domains (M1-M6) as defined by clustering of the velocities at the depths of 40-120 km.

domains with the depth along the average velocity profiles at a shear-wave velocity of 4.2 km/s, which is the minimum shear-wave velocity of melt-free ultramafic materials (e.g., Delph et al., 2021). Figure 12a shows that the depth to $V_S=4.2$ km/s in domains C1-C5 is roughly similar to the average crustal thickness, following the reference line (slope=1). The crustal thickness for domain C6 is about 36 ± 7.5 km, with a large error bar (Figure 12a-b). This may result from the fact that domain C6 spans across the PIE line, south of which the values are the depth to the plate interface, which dips to the north and thus varies significantly (Figure 11b). The same explanation is applicable to the crustal thickness for domain M5, which also has a large error bar (Figure 12c).

The clustering analysis in this study focuses on the holistic patterns of velocity profiles and, thus, crustal thickness information is implicitly considered. Crustal thickness clearly plays a role in defining the crustal domains. For example, domains C1 and C2 have thicker crusts, relative to C3, C4, and C5, and the uncertainties for C2 and C4 do not overlap (Figure 12b). However, the difference in the internal velocity structure of the crust is also significant. For example, C1 and C2 have mean crustal thicknesses that differ by less than 3 km (Figure 12b), but these domains have contrasting velocity profiles, with C2 containing lower velocities in the crust below 20 km depth (Figure 10c). On the other hand, domains C3, C4, and C5 in the central latitudes of Alaska have similar crustal thicknesses and similar internal velocity structures. These cases highlight the fact that the average velocity profiles from all models (Figure 10c) oversimplify some aspects of the crustal structure. The boundaries of C3, C4, and C5 were defined using the velocity profile clusters from at least three individual studies (Figure 10a), indicating that contrasts in velocity profiles between these domains do exist in some individual models. This result is backed up by the comparison of the cluster profiles for individual models (Figure S7), which indicates more complicated internal velocity heterogeneity. However, when the profiles of all models are averaged (Figure 10c), some of these differences are less evident. Average crustal thicknesses are also shown for the mantle domains (Figure 12c). With velocities from depths of 40-120 km, the mantle velocity clustering should be much less influenced by the variation of crustal thicknesses, which are <40 km in most of the study area (Figure 11b).

553 **5.2 Mantle heterogeneity of the seismic domains**

554 The mantle seismic structural domains possess distinctly different velocity structures,
 555 associated with varying lithospheric thicknesses, and in some cases with the influence of
 556 the subducting lithosphere. Comparison of the average velocity profiles in these domains
 557 indicates that mantle structure in Alaska can be divided into three broad domains: northernmost
 558 Alaska (M1), mantle containing subducting lithosphere in the south (M5), and
 559 everything in between (M2-M4 and M6).

560 Domain M1, in northernmost Alaska, is in a passive continental margin setting (e.g.,
 561 Colpron et al., 2007; Müller et al., 2019), and its outline approximately matches the North
 562 Slope subterrane of the Arctic Alaska terrane (AA_ns in Figure 13a; Plafker & Berg, 1994;
 563 Colpron et al., 2007). The M1 domain is distinguished by the thickest mantle lithosphere
 564 with the highest velocity found in Alaska (Figure 10d), matching the conclusions of a wide
 565 range of studies (O'Driscoll & Miller, 2015; Martin-Short et al., 2018; Jiang et al., 2018; Feng
 566 & Ritzwoller, 2019; Berg et al., 2020; Gama et al., 2021, 2022a, 2022b). Heat flow is low
 567 relative to the rest of Alaska over much of the M1 domain, consistent with the low vertical
 568 thermal gradient in a thick mantle lithosphere (Batir et al., 2016). However, intriguingly,
 569 heat flow appears to increase in the northernmost tip of M1 (Batir et al., 2016). The M1
 570 domain is also largely devoid of seismicity (Ruppert & West, 2020), suggesting little ongoing
 571 internal deformation. Most of the M1 domain lies beneath the relatively thick crust of the
 572 C1 crustal velocity domain, which is bordered by the thicker and lower-velocity crust of
 573 the C2 domain to the south (Figures 10 and 12b). The C2 domain largely corresponds
 574 to the Hammond-Coldfoot subterrane of the Arctic Alaska terrane (AA_h in Figure 13a)
 575 and the moderately high topography of the Brooks Range. Overall, these observations are
 576 consistent with geologic information that the M1 domain/North Slope Arctic Alaska terrane
 577 represents an anomalous continental terrane (Hubbard et al., 1987; Plafker & Berg, 1994;
 578 Colpron et al., 2007; Strauss et al., 2013) that experienced crustal shortening and thickening
 579 at its southern margin during its accretion. However, the new information provided by the
 580 analyses of EarthScope TA data clearly shows that the mantle lithosphere of this terrane is
 581 as distinctive as its crust, based on its large thickness, high velocities, and apparently low
 582 temperatures.

583 The overriding lithosphere over most of the rest of Alaska is relatively thin. Domains
 584 M2-4 and M6 show local minimum velocities at depths of 90-110 km, consistent with litho-
 585 sphere that ends above this depth (e.g., Martin-Short et al., 2018; Gama et al., 2022a, 2022b)
 586 (Figure 10d). The decrease of velocity for M4 within this depth range (90-110 km) is subtle
 587 but visible. This thinner lithosphere with an asthenospheric low-velocity layer is consistent
 588 with the higher heat flow observed in these domains (Batir et al., 2016). The lowest average
 589 asthenospheric velocities are observed in domains M2 and M6. M2 spans across the back-arc
 590 mantle of the main Alaska subduction zone. It reaches all the way to the Seward Peninsula
 591 where magmatic centers with decompression melting compositions occur (e.g., Mukasa et
 592 al., 2007). Domain M6, which also manifests the lowest average mantle lithospheric veloc-
 593 ities, is located to the northeast of the Wrangell Volcanic Field. It may also reflect melting
 594 in the back-arc mantle to the northeast of the Wrangell slab, characterized by the dipping
 595 seismicity and slab-alike high velocities (Yang & Gao, 2020; Daly et al., 2021; Mann et al.,
 596 2022). The lower velocities could be explained by the mobile back-arc tectonics (Hyndman
 597 et al., 2005) or the toroidal return flow around the eastern Alaska slab edge (Jadamec &
 598 Billen, 2010, 2012). Domain M4 spans across the North America basinal strata and the
 599 Yukon-Tanana terrane (Figure 13b) with a nearly constant average velocity of 4.4 km/s in
 600 the mantle lithosphere (Figure 10d). The abundance of velocity cluster boundaries in M4
 601 without clear lineaments (Figure 10b) suggests a highly heterogeneous mantle lithosphere
 602 in this region with strong lateral variations. M4 also overlaps with the northern corner of
 603 the shallowly subducting Yakutat Microplate (Figure 14; Hayes et al., 2018; Finzel, Flesch,
 604 Ridgway, Holt, & Ghosh, 2015; G. L. Pavlis et al., 2019), where a high-velocity body-wave
 605 anomaly is imaged (Figure 14). Additionally, M4 is located at the frontier of the Tintina

Fault that intersects with the west-southwest to east-northeast trending Kaltag Fault (e.g., Gabrielse et al., 2006; Audet et al., 2019; Esteve et al., 2020). Therefore, the strong lateral heterogeneity in M4 likely reflects a complex and highly deformed mantle lithosphere related to Yakutat Microplate subduction and its impact on upper plate deformation.

In contrast to the other mantle domains, M5, which lies within the footprint of the subducting lithosphere, does not on average show evidence of a well-developed layer of high-velocity mantle lithosphere (Figures 10d and 14). Rather, velocities remain relatively low above the depth of about 55 km (Figure 10d), likely representing the vertical juxtaposition of the overriding crust and that of the subducting plate, where the latter largely comprises a thick Yakutat oceanic plateau (e.g., G. L. Pavlis et al., 2019; Chuang et al., 2017; Rondenay et al., 2010). The continued velocity increase likely represents the transition to the mantle of the subducting plate, which dominates the average velocity profile down to depths of 120 km (Figure 10d).

5.3 Correlation of seismic domains with tectonic features

Many of the most prominent boundaries delineated by the clustering analysis of the velocity models strike approximately parallel to the trends of the tectonic terranes and major faults in Alaska (Figure 13). In southern Alaska, some of these trends are approximately east-west but concave to the south, parallel to the active convergent margin (e.g. domains C6 and M5). In northern Alaska, some structural trends are concave to the north (e.g. C1-C3), reflecting more ancient accretionary tectonic terranes. The velocity model clustering and crustal thickness analyses indicate that the Denali Fault System, the Kobuk Fault Zone, and potentially the Porcupine Shear Zone represent lithospheric-scale boundaries that separate regions with distinct seismic structures. In contrast, the relationships of the Kaltag and Tintina faults to crustal and mantle domains are more complex. These findings are described below.

The dextral strike-slip Denali Fault System in southern Alaska has long been the target of geophysical studies. With a well-documented 10-km northward thinning of the crust across the Denali Fault System and/or Hines Creek Fault (Figure 11b; Rossi et al., 2006; Veenstra et al., 2006; Brennan et al., 2011; Ward & Lin, 2018; Allam et al., 2017; Miller et al., 2018; Martin-Short et al., 2018; Haney et al., 2020; Mann et al., 2022; Gama et al., 2022a, 2022b), the overall Denali Fault System acts as a major crustal boundary that separates the Alaska Range and the Wrangellia composite terrane to the south and the North American affinity terranes in the interior of Alaska to the north (W. Nokleberg et al., 2013; Benowitz et al., 2022). High-resolution finite-element models of Alaska that incorporated a Denali fault lithospheric shear zone (Jadamec et al., 2013; Haynie & Jadamec, 2017) found a better fit to surface motion and regions of exhumation and subsidence in south-central Alaska than models that did not include a Denali fault shear zone (Jadamec & Billen, 2010, 2012). This suggests that the Denali Fault System may also represent a mantle structural boundary (Jadamec et al., 2013; O'Driscoll & Miller, 2015; Haynie & Jadamec, 2017; Gama et al., 2022b). For example, recent work by Gama et al. (2022b) found a northward increase in total lithospheric thickness across the Denali Fault System, which in many places is accompanied by an increase in the shear-wave velocity of the mantle lithosphere.

The velocity clustering analysis in this study corroborates the view that the Denali Fault System is a major structural boundary in both the crust and the mantle (Figure 13). In the crust, the Denali Fault System aligns with the northern margin of domain C6. The fault-correlated transition in crustal structure delineated by the northern C6 margin is largely related to the well-documented decrease in crustal thickness across the Denali Fault System (e.g. Figure 11b and the previous paragraph), although contrasts in crustal velocity may also contribute. For example, at the depths of <20 km, the C6 crust (south of the Denali Fault System) has a slightly higher velocity than the crust of the C4 and C5 domains (north of the Denali Fault System). However, while the transition from the C6 to

657 C4 or C5 domains does represent a significant change in crustal structure, the map of crustal
 658 thickness highlights that this transition is not uniform along the strike of the fault system.
 659 As noted in Section 4.4, the localization of the northward decrease in crustal thickness is
 660 most clearly correlated with the main trace of the Denali fault approximately east of 146°W.
 661 It is distributed across the Denali and Hines Creek Faults between 146–150°W and becomes
 662 more gradual and less well-correlated with the Denali Fault System west of 150°W. In the
 663 mantle, the Denali Fault System lies at the southern boundary of domains M4 and M6,
 664 where they transition to domain M5. The southern boundary of the M4 domain does not
 665 reach the western end of the Denali Fault System (Figure 13b). Instead, it terminates at the
 666 boundary that marks the eastern edge of the M2 domain at a longitude of approximately
 667 153°W, which corresponds to the edge of the high-velocity subducting lithosphere (Figure

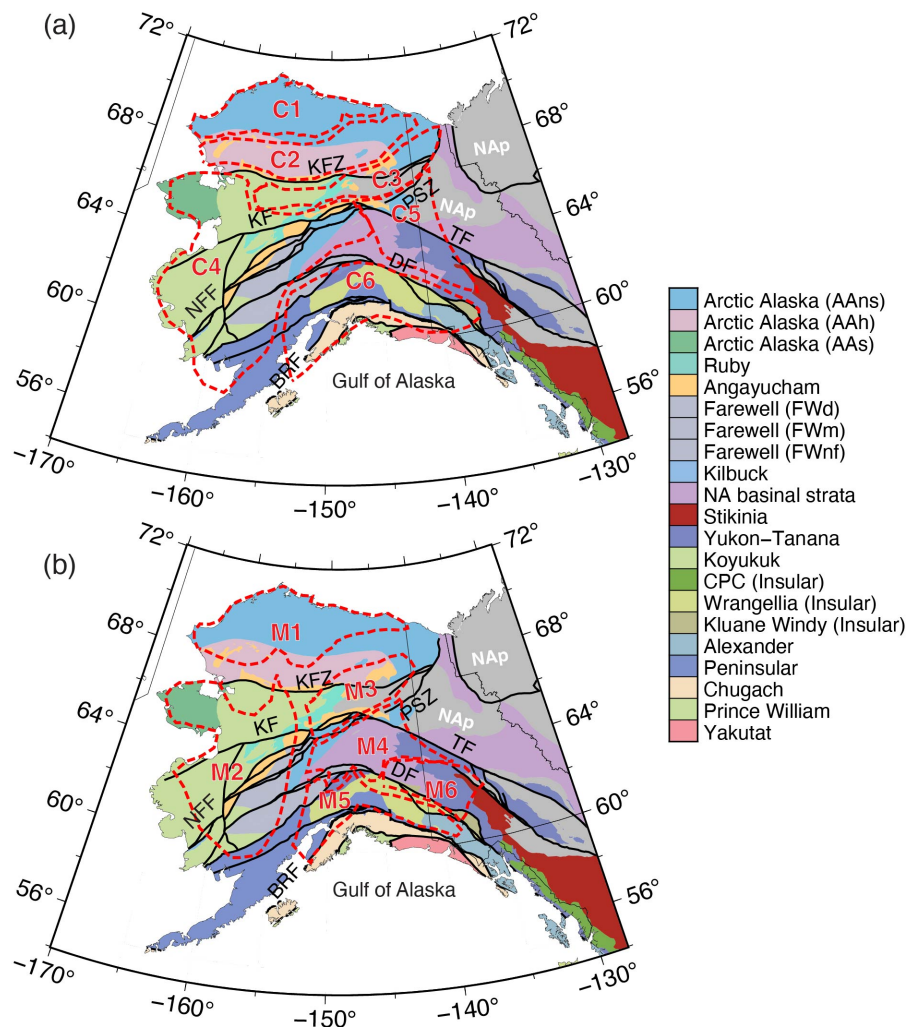


Figure 13. Comparison of velocity domains and major faults and tectonic terranes. (a) Major boundary lineaments of the velocity clusters (red dashed lines) and velocity domains (C1-C6) for 10-50 km clustering results overlapping on major fault lines and tectonic terrane maps. (b) Same as (a) but for mantle lithosphere at depths of 40-120 km (M1-M6). Labels of major faults are the same as in Figures 1b and 7 but are included here for easy reference. KFZ - Kobuk Fault Zone, KF - Kaltag Fault, PSZ - Porcupine Shear Zone, NFF - Nixon Fork-Iditarod Fault, TF - Tintina Fault, DF - Denali Fault System, BRF - Border Range Fault.

668 14). This relationship suggests that the cluster analysis in the 40-120 km depth range is
 669 strongly influenced by the subducting oceanic lithosphere in this region. To more directly
 670 assess mantle velocity contrasts across the Denali Fault System, where the overall lithosphere
 671 is relatively thin, velocity structure in the 50 km to 90 km depth range should be examined.
 672 For example, in this depth range, Gama et al. (2022b) found northward thickening of the
 673 lithosphere and/or a southward increase in mantle velocity across the Denali Fault System
 674 at longitudes of 154°W and further east, while such mantle contrasts are less prominent
 675 across the Denali Fault further to the west.

676 The east-west trending Kobuk Fault Zone to the south of the Brooks Range in northern
 677 Alaska is currently the site of low-rate dextral strike-slip motion (Elliott & Freymueller,
 678 2020) with a mix of faulting styles developed over time (Avé Lallement et al., 1998). How-
 679 ever, it has also been proposed as the ancient collisional boundary between the North Alaska
 680 Microplate to the north (including the North Slope and Hammond-Coldfoot subterranea)
 681 and the volcanic arc and other terranes to the south (Hubbard et al., 1987). The crustal
 682 thickness increases from 34 ± 3 km (C3) to 40 ± 3 km from south to north across the Kobuk
 683 Fault Zone (Figures 11b and 12b; Woppard et al., 1960; Clarke & Silver, 1991; Fuis et al.,
 684 1995, 1997; Searcy et al., 1996; Veenstra et al., 2006; Brennan et al., 2011; Allam et al.,
 685 2017; Miller et al., 2018; Zhang et al., 2019; Haney et al., 2020; Gama et al., 2021, 2022b,
 686 2022a). As described in Section 5.2, the velocity clustering results indicate the Kobuk Fault
 687 Zone lies at the boundary of major velocity domains, including the C2-C3, and M1-M3 transi-
 688 tions (Figures 10a-b and 13). This observation is consistent with the view that lithospheric
 689 structural gradients help to localize deformation on this fault system.

690 To the southeast of the Brooks Range, the southwest-northeast trending Porcupine
 691 Shear Zone, with evidence of sinistral movement (von Gosen et al., 2019), is the boundary
 692 between the North Slope subterranea of the Arctic Alaska terrane (AAns in Figure 13) and
 693 the North America platformal strata in western Laurentia (NAp in Figure 13; Colpron et
 694 al., 2007). Although smaller in scale compared to the Kobuk Fault Zone and the Denali
 695 Fault System, the Porcupine Shear Zone appears to be the structural boundary between
 696 both the crustal and mantle velocity domains (C3-C5 in Figures 10a and 13a and M3-M4 in
 697 Figure 10b and 13b). It also lies at a gradient in crustal thickness (Figure 11b). Thus the
 698 Porcupine Shear Zone is potentially a third strike-slip fault zone that connects to structural
 699 gradients in the mantle lithosphere.

700 In contrast, structural differences across the Kaltag Fault are primarily within the
 701 crustal range, while the structural signature of the Tintina Fault is primarily noticeable
 702 in the mantle lithosphere (Figure 13). The Kaltag Fault along the southern margin of the
 703 Brooks Range is a dextral strike-slip fault with more than 500 km slip in the late Cretaceous
 704 (Jones, 1980). Together with the Porcupine Shear Zone to its northeast, the Kaltag Fault
 705 has played an important role in the tectonic evolution of the Arctic Ocean Basin (Jones,
 706 1980). The velocity domains C3 and C4 are separated by a lineament of cluster boundaries
 707 along the eastern section of the Kaltag Fault, to the east of longitude 155°W (Figures 10a
 708 and 13a). This is also the section with different tectonic terranes on the two sides of the
 709 fault (Figure 13a). The structural contrast further west across the fault is ambiguous, which
 710 is consistent with the fact that both sides of the fault belong to the same Koyukuk tectonic
 711 terrane (Figure 13a).

712 The Tintina Fault in eastern Alaska and western Canada is a margin-parallel, dextral
 713 strike-slip fault zone with about 430 km horizontal displacement (e.g., Gabrielse et al.,
 714 2006). Audet et al. (2019) and Esteve et al. (2020) imaged a prominent contrast in seismic
 715 velocities in the upper mantle across the Tintina Fault in the western Yukon, suggesting
 716 the fault as a lithospheric-scale shear zone along the western margin of the North American
 717 continent. In the velocity clustering results, a small section of the Tintina Fault coincides
 718 with the northwest-southeast trending northeastern edges of the M4 and M6 mantle domains
 719 (Figure 13b). In the individual N2020, F2019, J2018, and W2018 models, an anomalously
 720 high-velocity mantle lithosphere lies beneath the Yukon Stable Block, which is referred to

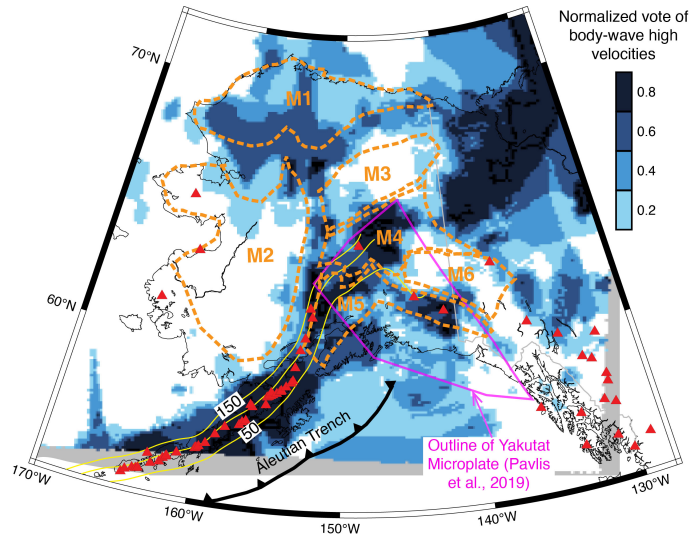


Figure 14. Comparison of mantle lithospheric velocity domains (M1-M6 within dashed outlines) and body-wave high velocities vote map at the depth of 100 km (colored background). The body-wave high-velocity vote map is from Pavlis et al. (this book), which contains more details on the body-wave vote maps. The slab depth contours (yellow lines with labeled depths in km) are from Slab 2.0 (Hayes et al., 2018). The outline of the Yakutat Microplate (magenta polygon) is from G. L. Pavlis et al. (2019). The red triangles are the active volcanoes same as in Figure 1a.

by Esteve et al. (2020) as the Mackenzie craton. It is a fragment of the North American Platform on the northeast side of the Tintina Fault. However, the fault does not align with crustal cluster boundaries (Figure 13a). In summary, our analyses suggest that contrast in seismic structure exist mostly across a segment of the Tintina Fault in the mantle. This result, however, does not rule out a more laterally persistent contrast of seismic velocities at specific depths, since the clustering analysis considers the average pattern over the 40-120 km depth range.

Velocity domains C6 and M5 are both spatially correlated with the Wrangellia composite terrane, sampling both continental and oceanic lithosphere (Figure 13). At depths of 10-50 km, domain C6 contains varying amounts of both overriding crust and the oceanic lithosphere of the downgoing Yakutat Microplate. The average velocity below the depth of about 25 km is much lower than those for the adjacent C4-C5 domains (Figure 10c). This might be attributed to the inclusion of the overriding crust and the underlying thick (up to 25 km) oceanic crust of the downgoing Yakutat Microplate (Eberhart-Phillips et al., 2004; Rondenay et al., 2010; Bauer et al., 2014; Chuang et al., 2017; Yang & Gao, 2020; Mann et al., 2022), resulting in combined crustal thicknesses that reach 55 km (Figure 11). As previously discussed (Section 5.2), at depths of 40-120 km in the M5 domain, the lower velocities than in other domains above the depth of 55 km likely reflect the thicker crust (Figure 10d), while the monotonically increasing velocities at greater depths sample mostly the oceanic mantle lithosphere (Rondenay et al., 2010; Yang & Gao, 2020; Gama et al., 2022a; Mann et al., 2022). The northern boundaries of the C6 and M5 domains approximately align with the northern edge of a zone where P-wave receiver functions show anomalously strong azimuthal signals that are diagnostic of dipping fabrics, either dipping boundaries between isotropic layers, or contrasts in P-wave velocity anisotropy where a plunging symmetry axis exists on at least one side of the interface (Schulte-Pelkum et al., 2020). This zone of intense dipping fabrics has been attributed to deformation related to subduction and oblique convergence (Schulte-Pelkum et al., 2020). Zones with prominent dipping fabrics also occur in portions

748 of the C1 and M1 domains in northernmost Alaska (Schulte-Pelkum et al., 2020), but there
 749 the spatial variations in the intensity of the dipping fabrics are not well-correlated with the
 750 C1 and M6 boundaries.

751 **5.4 Implications for the tectonics and geodynamics of the overriding conti-**
 752 **nental lithosphere**

753 This study reveals a number of seismic features of the Alaskan crust and mantle as
 754 highlighted by the shear-wave velocity model clustering and the integration of crustal thick-
 755 ness estimates. These seismic features shed light on the direction of future seismic, tectonic,
 756 and geodynamical studies, considering that variations in upper plate structure can have a
 757 first-order effect on both deformation in the overriding plate as well as the dynamics of the
 758 subducting slab (e.g. Sharples et al., 2014; Jadamec & Billen, 2012; Haynie & Jadamec,
 759 2017).

760 One of the key findings from the synthesis is that some of the major faults and terrane
 761 boundaries spatially align with the margins of the crustal and mantle velocity domains that
 762 were independently determined from the velocity model clusters. Some of these correlations
 763 were previously documented, as in the case of the Denali and Kobuk faults (Rossi et al.,
 764 2006; Veenstra et al., 2006; Brennan et al., 2011; Ward & Lin, 2018; Allam et al., 2017;
 765 Miller et al., 2018; Martin-Short et al., 2018; Haney et al., 2020; Mann et al., 2022; Gama
 766 et al., 2022a, 2022b), but others, as in the case of the Porcupine Shear Zone, are newly
 767 revealed in this study. However, we have found that many boundaries of crustal and mantle
 768 velocity domains are not aligned. These results have the potential to add new constraints to
 769 tectonic models for how the complex mosaic of Alaskan terranes and faults interact (Bird,
 770 1996; Kalbas et al., 2008; Elliott & Freymueller, 2020) and how they have evolved over
 771 time. A key next step will be to isolate how much of the mantle heterogeneity captured
 772 in the 40–120 km clusters actually lies within the mantle lithosphere, versus the underlying
 773 asthenosphere or subducting plate.

774 In the case of northernmost Alaska, the southern boundary of the M1 domain corre-
 775 sponds to a lithospheric-scale feature that separates the anomalously thick and high-velocity
 776 mantle lithosphere beneath the North Slope Arctic Alaska terrane from the thinner litho-
 777 sphere to the south. This observation poses a number of interesting questions. How has the
 778 North Slope M1 mantle lithosphere maintained its distinctive thickness and internal velocity
 779 structure over time? How much of the high mantle velocity is due to temperature, and how
 780 much could be attributed to mantle composition? A high-resolution model of mantle attenu-
 781 ation would be helpful in resolving this latter point, while the former requires input from
 782 geodynamic modeling efforts. Does the high velocity of the North Slope mantle actually
 783 signify a fragment of cratonic mantle lithosphere, as suggested in some studies (Gama et
 784 al., 2022b), and does this indicate that the C1 domain is a remnant cratonic crust? The
 785 C2 domain, which contains the Brooks Range and lies over a transitional mantle with a
 786 variable lithospheric thickness, is comparable to many continental orogenic belts worldwide.
 787 How much does the anomalously thick and low-velocity (Figure 10c) C2 crust isostatically
 788 support the Brooks Range, versus isostatic contributions from the mantle? Geodynamic
 789 modeling studies thus far have led to significant advances in understanding the tectonics of
 790 Alaska and the surrounding regions, but much remains to be learned. Three-dimensional
 791 finite-element models spanning the entirety of mainland Alaska and northwestern Canada
 792 have incorporated a laterally variable lithospheric structure in the overriding plate, though
 793 focusing on the deformation in central and southern Alaska (Bird, 1996; Kalbas et al., 2008;
 794 Jadamec & Billen, 2010; Jadamec et al., 2013). However, these models are limited by ei-
 795 ther not including the asthenosphere (e.g. Bird, 1996; Kalbas et al., 2008) or including the
 796 asthenosphere and part of the lower mantle but essentially fixing the North Slope region
 797 to the model boundary and, thus, limiting the lithospheric motion in northernmost Alaska
 798 (e.g. Jadamec & Billen, 2010; Jadamec et al., 2013). Other numerical models have included
 799 the deformation of northern Alaska using a thin viscous sheet approach (e.g. Finzel et al.,

800 2015). However, the think viscous sheet models do not solve for flow in the asthenosphere
 801 or lower mantle. In the future, a more complete treatment of the North Slope region will
 802 aid in self-consistently assessing mantle flow and Brooks Range equilibrium, for example.
 803 Overall, the new EarthScope data and results will foster continued rich model development
 804 and geodynamic discovery in Alaska and northwestern Canada.

805 The alignment of some major fault systems (Denali, Kobuk, Porcupine Shear Zone,
 806 Kaltag, Tintina) with the margins of the crustal and/or mantle velocity domains also has
 807 the potential to provide new constraints on the depth extent and dynamics of strike-slip
 808 faulting in the continental lithosphere. Such correlations may indicate that lateral variations
 809 in the strength of the crust and mantle lithosphere play a role in determining and
 810 maintaining the location of the fault zone, as has been suggested globally (e.g., Molnar &
 811 Dayem, 2010; Dayem et al., 2009). The fault zones and the local reduction in strength
 812 that they represent in turn have a major impact on the dynamics of the overriding plate
 813 in Alaska (e.g., Haynie & Jadamec, 2017). For example, the Wrangell block, a region
 814 between the Alaska megathrust to the south and the Denali fault to the north, moves semi-
 815 independently from the inboard North American plate of interior Alaska (Lahr & Plafker,
 816 1980). GPS data analyses indicate the northwest-directed counter-clockwise motion of the
 817 Wrangell block and its subdomains (e.g. Elliott & Freymueller, 2020). Geodynamic mod-
 818 eling demonstrates that the sub-parallelism of the plate boundary corner with the inboard
 819 Denali fault allows northwest-directed flat slab subduction of the Pacific-Wrangell plate to
 820 drive the overriding Wrangell block from below, with the Denali fault strength modulating
 821 its rotation (Jadamec et al., 2013; Haynie & Jadamec, 2017). In the future, high-resolution
 822 studies of seismic velocity (both isotropic and anisotropic) in the vicinity of the major
 823 fault systems of Alaska have the potential to help constrain this process and the degree to
 824 which strike-slip deformation remains horizontally localized in the deep crust and mantle
 825 lithosphere.

826 The results of this study also highlight the significant effect of the subduction of the
 827 Yakutat terrane in southern Alaska, which is expressed as the thick crust evident in the
 828 C6 and the top of the M5 domains, and the structural complexity in the M4 domain. The
 829 average crustal velocity profile in the C6 domain (which reflects continental crust over the
 830 subducting plate) provides new constraints on the buoyancy of the Yakutat crust. These
 831 constraints will be useful for lithospheric-scale (e.g., Finzel et al., 2015; McConeghy, Flesch,
 832 & Elliott, 2022) and mantle-scale (e.g., Jadamec & Billen, 2010, 2012; Jadamec et al., 2013;
 833 Haynie & Jadamec, 2017) geodynamical models of subduction in Alaska and its impact
 834 on the overriding continental lithosphere. The crustal seismic velocities and thickness con-
 835 straints synthesized in this study could also help to better design representative models of
 836 upper plate dynamics (Torne et al., 2019) and models of plateau subduction to examine the
 837 effects of plateau subduction-collision on long-term plate boundary evolution (e.g., Koons et
 838 al., 2010; Haynie, 2019; Moresi et al., 2014) and the role of eclogitization of the subducting
 839 plateau with depth (Arrial & Billen, 2013).

840 6 Conclusions

841 A primary goal of this study was to synthesize the results of existing seismic studies
 842 to create tools for studying the upper plate lithosphere in Alaska that could be used by a
 843 broad range of researchers. To that end, this study provides:

- 844 • Maps showing the results of seven studies of crustal thickness based on receiver func-
 tions;
- 845 • A crustal thickness reference map that synthesizes the three of these crustal thick-
 ness models that provided at least semi-continuous sampling, and that accounts for
 complexity due to multiple crustal layers in southern Alaska;
- 846 • Maps of eight published shear-velocity models for Alaska;

- Domain boundaries determined through clustering analysis and their corresponding velocity profiles from the individual shear-velocity models;
- Composite domain boundaries and mean velocity profiles that represent the combination of all shear-velocity models.

Through the clustering analysis, six distinct velocity domains are identified in the crustal depth range (10-50 km) and in the mantle (40-120 km), without considering information on the distribution of terranes and faults. However, the velocity domain boundaries are in many cases close to terrane boundaries and/or major fault systems, indicating feedback between the crust (and even mantle structure) and geologic features at the surface. These correlations include both crust and mantle domain boundaries that align with: the Denali Fault System and the boundary between the Wrangellia composite terrane and interior Alaska; the Kobuk fault and the southern boundary of the Hammond-Coldfoot subterrane in northern Alaska; the southern boundary of the North Slope subterrane in northern Alaska; and the Porcupine Shear Zone in northern Alaska. The Kaltag Fault and the Tintina Fault at least partially align with the crustal and mantle velocity domain boundaries, respectively.

The crust and mantle velocity domains clearly outline three major structural domains within the upper plate of Alaska: the anomalously thick crust associated with the subduction of the Yakutat terrane in the south; the thin lithosphere above a well-defined low-velocity lithosphere over much of interior Alaska; an anomalously thick crust and a transition to thicker lithosphere beneath the Brooks Range; and a thick crust above very thick and high-velocity mantle lithosphere beneath the North Slope subterrane in northernmost Alaska. The western edge of the thick lithosphere beneath the MacKenzie craton in Canada is also detected as a mantle domain boundary.

Availability Statement

Seismic network information is available from the IRIS Data Management Center (<https://ds.iris.edu/ds/nodes/dmc/>) and the International Federation of Digital Seismograph Networks (<https://www.fdsn.org>). The network codes and digital object identifiers (DOI) are: 5C (DOI:10.7914/SN/5C_2009), 7C (DOI:10.7914/SN/7C_2015), AK (DOI:10.7914/SN/AK), AT (DOI:10.7914/SN/AT), AV (DOI:10.7914/SN/AV), CN (DOI:10.7914/SN/CN), II (DOI:10.7914/SN/II), IM (no DOI), IU (DOI:10.7914/SN/IU), PP (no DOI), PQ (DOI:10.7914/SN/PQ), TA (DOI:10.7914/SN/TA), US (DOI:10.7914/SN/US), XE (DOI:10.7914/SN/XE_1999), XF (DOI:10.7914/SN/XF_2009), XL (DOI:10.7914/SN/XL_2008), XM (DOI:10.7914/SN/XM_2011), XN (DOI:10.7914/SN/XN_2003), XO (DOI:10.7914/SN/XO_2018), XR (DOI:10.7914/SN/XR_2004), XV (DOI:10.7914/SN/XV_2014), XZ (DOI:10.7914/SN/XZ_2005), YE (DOI:10.7914/SN/YE_2007), YG (DOI:10.7914/SN/YG_2016), YM (DOI:10.7914/SN/YM_2002), YO (DOI:10.7914/SN/YO_2010), YV (DOI:10.7914/SN/YV_2006), Z5 (DOI:10.7914/SN/Z5_2018), ZE (DOI:10.7914/SN/ZE_2015). See Table S1 in the supplement for detailed descriptions and references of the seismic networks. The seismic models are downloaded from IRIS Earth Model Collaboration (<https://doi.org/10.17611/DP/EMC.1>) or directly provided by the corresponding authors. The clustering analysis of the seismic velocity models is conducted using *SeisGo* (<https://doi.org/10.5281/zenodo.5873724>). Figures 1, 2, 5, 6, 11, and 13 are created using the Generic Mapping Tools (Wessel et al., 2019). The electronic supplementary file for Figures S1-S9 and Table S1, the velocity domain outlines, the key cluster boundaries (cluster lineaments), the average crustal thickness models, and the Python Jupyter notebook to plot the cluster domains are archived on Zenodo and can be downloaded from <https://doi.org/10.5281/zenodo.7516572>.

Acknowledgments

This paper grew out of discussions at the UNAVCO Alaska EarthScope and Beyond Virtual Seminar Series in Spring 2021 and the paired EarthScope Alaska and Beyond Virtual

900 Workshop in May 2021, which were supported by the National Science Foundation and the
901 National Aeronautics and Space Administration. The authors thank the conference organiza-
902 nizers, Jeffrey Freymueller, Julie Elliot, Sarah Roeske, and Rick Aster, and participants at
903 the meeting for thoughtful discussions. We are also grateful to R. Martin-Short, M. Miller,
904 and A. Li for directly providing their models, to the other authors who made their models
905 available through the IRIS EMC, and to the field teams for deploying and maintaining the
906 seismic networks used to produce the synthesized seismic models. We appreciate the con-
907 structive comments from the editor (Natalia Ruppert), Xueyang Bao, Carl Tape, and an
908 anonymous reviewer that significantly improved the manuscript. X. Yang thanks Chuan-
909 ming Liu for providing the script to plot the tectonic terranes in Figures 1b and 13. This
910 work is supported by the startup funding of Purdue University to X. Yang, NSF CAREER
911 Award NSF-EAR 1945513 to M. Jadamec, NSF EAR-2052558 to S. S. Wei, NSF EAR-
912 2053042 and Woods Hole Oceanographic Institution OBS Instrument Center Postdoctoral
913 Scholarship to M. E. Mann, and NSF EAR-1829401 to K. M. Fischer. **Author Contribu-**
914 **tions:** X. Yang contributed to supervision, funding acquisition, data curation, methodology,
915 formal analysis, interpretation, and writing of the original draft. M. Mann and K. Fischer
916 contributed to data curation, methodology, formal analysis, interpretation, and writing of
917 the original draft. M. Jadamec contributed to the contextual outlining and writing of the
918 original draft. S. Wei and A. Schaeffer contributed to methodology. G. Pavlis contributed
919 to formal analysis. All authors contributed to the conceptualization, interpretation, and
920 reviewing and editing of the manuscript.

921 **References**

- 922 Ai, Y., Zhao, D., Gao, X., & Xu, W. (2005, 6). The crust and upper mantle discontinuity
 923 structure beneath Alaska inferred from receiver functions. *Physics of the Earth and*
 924 *Planetary Interiors*, *150*, 339-350. doi: 10.1016/J.PEPI.2004.12.002
- 925 Allam, A. A., Schulte-Pelkum, V., Ben-Zion, Y., Tape, C., Ruppert, N., & Ross, Z. E. (2017,
 926 11). Ten kilometer vertical Moho offset and shallow velocity contrast along the Denali
 927 fault zone from double-difference tomography, receiver functions, and fault zone head
 928 waves. *Tectonophysics*, *721*, 56-69. doi: 10.1016/J.TECTO.2017.09.003
- 929 Anderson, D. L. (1987, 5). A seismic equation of state II. Shear properties and ther-
 930 modynamics of the lower mantle. *Physics of the Earth and Planetary Interiors*,
 931 *45*, 307-323. Retrieved from <https://linkinghub.elsevier.com/retrieve/pii/0031920187900392> doi: 10.1016/0031-9201(87)90039-2
- 933 Arrial, P.-A., & Billen, M. I. (2013). Influence of geometry and eclogitization on oceanic
 934 plateau subduction. *Earth and Planetary Science Letters*, *363*, 34-43.
- 935 Audet, P., Currie, C. A., Schaeffer, A. J., & Hill, A. M. (2019). Seismic evidence for litho-
 936 spheric thinning and heat in the northern Canadian Cordillera. *Geophysical Research
 937 Letters*, *46*(8), 4249 - 4257.
- 938 Audet, P., Schutt, D. L., Schaeffer, A. J., Estève, C., Aster, R. C., & Cubley, J. F. (2020,
 939 11). Moho Variations across the Northern Canadian Cordillera. *Seismological Research
 940 Letters*, *91*, 3076-3085. doi: 10.1785/0220200166
- 941 Avé Lallement, H. G., Gottschalk, R. R., Sisson, V. B., & Oldow, J. S. (1998). Structural
 942 analysis of the Kobuk fault zone, north-central Alaska. *Special Paper of the Geological
 943 Society of America*, *324*, 261-268. doi: 10.1130/0-8137-2324-8.261
- 944 Barcheck, G., Abers, G. A., Adams, A. N., Bécel, A., Collins, J., Gaherty, J. B., ... Wor-
 945 thington, L. L. (2020, 11). The Alaska Amphibious Community Seismic Experiment.
 946 *Seismological Research Letters*, *91*, 3054-3063. doi: 10.1785/0220200189
- 947 Batir, J. F., Blackwell, D. D., & Richards, M. C. (2016). Heat flow and temperature-depth
 948 curves throughout Alaska: Finding regions for future geothermal exploration. *Journal
 949 of Geophysics and Engineering*, *13*, 366-377. doi: 10.1088/1742-2132/13/3/366
- 950 Bauer, M. A., Pavlis, G. L., & Landes, M. (2014). Subduction geometry of the Yakutat
 951 terrane, southeastern Alaska. *Geosphere*, *10*, 1161-1176. doi: 10.1130/GES00852.1
- 952 Benowitz, J. A., Roeske, S. M., Regan, S. P., Waldien, T. S., Elliott, J. L., & O'Sullivan,
 953 P. B. (2022, 6). Large-scale, crustal-block vertical extrusion between the Hines Creek
 954 and Denali faults coeval with slip localization on the Denali fault since ca. 45 Ma,
 955 Hayes Range, Alaska, USA. *Geosphere*, *18*, 1030-1054. Retrieved from <https://doi.org/10.1130/GES02466.1>. doi: 10.1130/GES02466.1
- 956 Berg, E. M., Lin, F. C., Allam, A., Schulte-Pelkum, V., Ward, K. M., & Shen, W.
 957 (2020, 2). Shear velocity model of Alaska via joint inversion of rayleigh wave el-
 958 lipticity, phase velocities, and receiver functions across the Alaska transportable ar-
 959 ray. *Journal of Geophysical Research: Solid Earth*, *125*, e2019JB018582. Retrieved
 960 from <https://onlinelibrary.wiley.com/doi/full/10.1029/2019JB018582> doi:
 961 10.1029/2019JB018582
- 962 Bird, P. (1996). Computer simulations of Alaskan tectonics. *Tectonics*, *15*(2), 225-236.
- 963 Bird, P. (2003). An updated digital model of plate boundaries. *Geochemistry Geophysics
 964 Geosystems*, *4*(3), 1027. doi: 10.1029/2001GC000252
- 965 Bostock, M. G. (2013, 12). The Moho in subduction zones. *Tectonophysics*, *609*, 547-557.
 966 doi: 10.1016/J.TECTO.2012.07.007
- 967 Brennan, P. R. K., Gilbert, H., Ridgway, K. D., Brennan, P. R. K., Gilbert, H., & Ridgway,
 968 K. D. (2011, 4). Crustal structure across the central Alaska range: Anatomy of a
 969 mesozoic collisional zone. *Geochemistry, Geophysics, Geosystems*, *12*, 4010. Retrieved
 970 from <https://onlinelibrary.wiley.com/doi/full/10.1029/2011GC003519> doi:
 971 10.1029/2011GC003519
- 972 Chuang, L., Bostock, M., Wech, A., & Plourde, A. (2017, 7). Plateau subduction, in-
 973 traslab seismicity, and the Denali (Alaska) volcanic gap. *Geology*, *45*, 647-650.
- 974

- 975 Retrieved from <https://pubs.geoscienceworld.org/geology/article/45/7/647-650/207873> doi: 10.1130/G38867.1
- 976
- 977 Clarke, T. J., & Silver, P. G. (1991, 1). A procedure for the systematic interpretation of body
978 wave seismograms—I. Application to Moho depth and crustal properties. *Geophysical*
979 *Journal International*, 104, 41-72. Retrieved from <https://academic.oup.com/gji/article/104/1/41/569865> doi: 10.1111/J.1365-246X.1991.TB02493.X
- 980
- 981 Colpron, M., Nelson, J. L., & Murphy, D. C. (2007, 4). Northern Cordilleran terranes
982 and their interactions through time. *GSA Today*, 17, 4. Retrieved from <http://www.geosociety.org/gsatoday/archive/17/4/pdf/i1052-5173-17-4-4.pdf> doi:
983 10.1130/GSAT01704-5A.1
- 984
- 985 Coney, P. J., Jones, D. L., & Monger, J. W. (1980). Cordilleran suspect terranes. *Nature*
986 1980 288:5789, 288, 329-333. Retrieved from <https://www.nature.com/articles/288329a0> doi: 10.1038/288329a0
- 987
- 988 Daly, K. A., Abers, G. A., Mann, M. E., Roecker, S., & Christensen, D. H. (2021,
989 11). Subduction of an oceanic plateau across southcentral Alaska: High-resolution
990 seismicity. *Journal of Geophysical Research: Solid Earth*, 126. Retrieved from
991 <https://onlinelibrary.wiley.com/doi/10.1029/2021JB022809> doi: 10.1029/
992 2021JB022809
- 993
- 994 Dayem, K. E., Houseman, G. A., & Molnar, P. (2009, 6). Localization of shear along a
995 lithospheric strength discontinuity: Application of a continuous deformation model
996 to the boundary between Tibet and the Tarim Basin. *Tectonics*, 28. Retrieved
997 from <https://onlinelibrary.wiley.com/doi/full/10.1029/2008TC002264> doi:
10.1029/2008TC002264
- 998
- 999 Delph, J. R., Shimizu, K., & Ratschbacher, B. C. (2021, 7). The architecture of the
1000 southern Puna Magmatic System: Integrating seismic and petrologic observations
1001 with geochemical modeling. *Journal of Geophysical Research: Solid Earth*, 126,
1002 e2020JB021550. Retrieved from <https://onlinelibrary.wiley.com/doi/full/10.1029/2020JB021550> doi: 10.1029/2020JB021550
- 1003
- 1004 DeMets, C., Gordon, R. G., Argus, D. F., & Stein, S. (1994). Effect of recent revisions to
1005 the geomagnetic reversal time scale on estimates of current plate motions. *Geophysical*
1006 *Research Letters*, 218(207-237), 2191-2194.
- 1007
- 1008 Eberhart-Phillips, D., Christensen, D. H., Brocher, T. M., Dutta, U., Hansen, R. J., &
1009 Ratchkovski, N. A. (2004). Imaging the transition from Aleutian subduction to Yakutat
1010 collision in central Alaska, with local earthquakes and active source data. *Geological*
1011 *Society of New Zealand Miscellaneous Publication*, 117A, 27.
- 1012
- 1013 Eberhart-Phillips, D., Christensen, D. H., Brocher, T. M., Hansen, R., Ruppert, N. A.,
1014 Haeussler, P. J., & Abers, G. A. (2006). Imaging the transition from Aleutian
1015 subduction to Yakutat collision in central Alaska, with local earthquakes and ac-
1016 tive source data. *Journal of Geophysical Research: Solid Earth*, 111, 1-31. doi:
10.1029/2005JB004240
- 1017
- 1018 Elliott, J., & Freymueller, J. T. (2020). A block model of present-day kinematics of Alaska
1019 and western Canada. *Journal of Geophysical Research: Solid Earth*, 125, 1-30. doi:
1020 10.1029/2019JB018378
- 1021
- 1022 Enkelmann, E., Zeitler, P., Garver, J., Pavlis, T., & Hooks, B. (2010). The thermochronolog-
1023 ical record of tectonic and surface process interaction at the Yakutat–North American
1024 collision zone in southeast Alaska. *American Journal of Science*, 310(4), 231–260.
- 1025
- 1026 Esteve, C., Audet, P., Schaeffer, A. J., Schutt, D., Aster, R. C., & Cubley, J. (2020). The up-
1027 per mantle structure of northwestern Canada from teleseismic body wave tomography.
1028 *Journal of Geophysical Research: Solid Earth*, 125(2).
- 1029
- Esteve, C., Gosselin, J., Audet, P., Schaeffer, A. J., Schutt, D., & Aster, R. C. (2021).
Surface-wave tomography of the Northern Canadian Cordillera using earthquake
Rayleigh wave group velocities. *Journal of Geophysical Research*, 126. Retrieved
from <https://doi.org/10.1029/2021JB021960>
- Eymold, W. K., & Jordan, T. H. (2019, 11). Tectonic regionalization of the southern
california crust from tomographic cluster analysis. *Journal of Geophysical Research:*

- 1030 *Solid Earth*, 124, 11840-11865. Retrieved from <https://agupubs.onlinelibrary.wiley.com/doi/10.1029/2019JB018423> doi: 10.1029/2019JB018423

1031 Falkowski, S., & Enkelmann, E. (2016, 8). Upper-crustal cooling of the Wrangellia composite terrane in the northern St. Elias Mountains, western Canada. *Lithosphere*, 8, 359-378. Retrieved from <http://pubs.geoscienceworld.org/gsa/lithosphere/article-pdf/8/4/359/3040051/359.pdf> doi: 10.1130/L508.1

1032 Feng, L., & Ritzwoller, M. H. (2019). A 3-D shear velocity model of the crust and uppermost mantle beneath Alaska including apparent radial anisotropy. *Journal of Geophysical Research: Solid Earth*, 124, 10468-10497. doi: 10.1029/2019JB018122

1033 Finzel, E. S., Flesch, L. M., Ridgway, K. D., Holt, W. E., & Ghosh, A. (2015). Surface motions and intraplate continental deformation in Alaska driven by mantle flow. *Geophysical Research Letters*, 42(11), 4350 - 4358.

1034 Fuis, G. S., Levander, A. R., Lutter, W. J., Wissinger, E. S., Moore, T. E., & Christensen, N. I. (1995). Seismic images of the Brooks Range, Arctic Alaska, reveal crustal-scale duplexing. *Geology*, 23, 65-68. Retrieved from <http://pubs.geoscienceworld.org/gsa/geology/article-pdf/23/1/65/4665573/i0091-7613-23-1-65.pdf>

1035 Fuis, G. S., Moore, T. E., Plafker, G., Brocher, T. M., Fisher, M. A., Mooney, W. D., ... Ruppert, N. A. (2008). Trans-Alaska Crustal Transect and continental evolution involving subduction underplating and synchronous foreland thrusting. *Geology*, 36, 267-270. doi: 10.1130/G24257A.1

1036 Fuis, G. S., Murphy, J. M., Lutter, W. J., Moore, T. E., Bird, K. J., & Christensen, N. I. (1997, 9). Deep seismic structure and tectonics of northern Alaska: Crustal-scale duplexing with deformation extending into the upper mantle. *Journal of Geophysical Research: Solid Earth*, 102, 20873-20896. Retrieved from <https://onlinelibrary.wiley.com/doi/full/10.1029/96JB03959> doi: 10.1029/96JB03959

1037 Fuis, G. S., & Plafker, G. (1991, 3). Evolution of deep structure along the Trans-Alaska Crustal Transect, Chugach Mountains and Copper River Basin, southern Alaska. *Journal of Geophysical Research: Solid Earth*, 96, 4229-4253. Retrieved from <https://onlinelibrary.wiley.com/doi/full/10.1029/90JB02276> doi: 10.1029/90JB02276

1038 Gabrielse, H., Murphy, D. C., & Mortensen, J. K. (2006). Cretaceous and Cenozoic dextral orogen-parallel displacements, magmatism, and paleogeography, north-central Canadian Cordillera. In J. Haggart & J. E. R.J.Monger (Eds.), *Paleogeography of the north american cordillera: Evidence for and against large-scale displacements: Geological association of canada special paper* (Vol. 46, p. 255-276). Retrieved from <https://www.researchgate.net/publication/285873017>

1039 Gama, I., Fischer, K. M., Dalton, C. A., & Eilon, Z. (2022b, 12). Variations in Lithospheric Thickness across the Denali Fault and in Northern Alaska. *Geophysical Research Letters*, e2022GL101256. Retrieved from <https://onlinelibrary.wiley.com/doi/full/10.1029/2022GL101256> doi: 10.1029/2022GL101256

1040 Gama, I., Fischer, K. M., Eilon, Z., Krueger, H. E., Dalton, C. A., & Flesch, L. M. (2021, 4). Shear-wave velocity structure beneath Alaska from a Bayesian joint inversion of Sp receiver functions and Rayleigh wave phase velocities. *Earth and Planetary Science Letters*, 560, 116785. doi: 10.1016/J.EPSL.2021.116785

1041 Gama, I., Fischer, K. M., & Hua, J. (2022a, 10). Mapping the lithosphere and asthenosphere beneath Alaska with Sp converted waves. *Geochemistry, Geophysics, Geosystems*, 23, e2022GC010517. Retrieved from <https://onlinelibrary.wiley.com/doi/10.1029/2022GC010517> doi: 10.1029/2022GC010517

1042 Gou, T., Zhao, D., Huang, Z., & Wang, L. (2019). Aseismic deep slab and mantle flow beneath Alaska: Insight from anisotropic tomography. *Journal of Geophysical Research: Solid Earth*, 124, 1700-1724. doi: 10.1029/2018JB016639

1043 Grantz, A., May, S. D., & Hart, P. E. (1994). Geology of the Arctic continental margin of Alaska. In *The Geology of Alaska* (Vols. DNAG, Geology of North America). Geological Society of America. doi: 10.1130/DNAG-GNA-G1.17

1044 Haney, M. M., Ward, K. M., Tsai, V. C., & Schmandt, B. (2020, 11). Bulk struc-

- ture of the crust and upper mantle beneath Alaska from an approximate Rayleigh-wave dispersion formula. *Seismological Research Letters*, 91, 3064-3075. Retrieved from <https://pubs.geoscienceworld.org/ssa/srl/article/91/6/3064/589671/Bulk-Structure-of-the-Crust-and-Upper-Mantle> doi: 10.1785/0220200162
- Hayes, G. P., Moore, G. L., Portner, D. E., Hearne, M., Flamme, H., Furtney, M., & Smoczyk, G. M. (2018). Slab2, a comprehensive subduction zone geometry model. *Science*, 362, 58-61. doi: 10.1126/science.aat4723
- Haynie, K. L. (2019). *Controls of flat slab versus oceanic plateau subduction on overriding plate deformation in south-central Alaska* (Unpublished doctoral dissertation). State University of New York at Buffalo.
- Haynie, K. L., & Jadamec, M. A. (2017, 7). Tectonic drivers of the Wrangell block: Insights on fore-arc sliver processes from 3-D geodynamic models of Alaska. *Tectonics*, 36, 1180-1206. Retrieved from <https://onlinelibrary.wiley.com/doi/10.1002/2016TC004410> doi: 10.1002/2016TC004410
- Hubbard, R. J., Edrich, S. P., & Rattey, R. P. (1987, 2). Geologic evolution and hydrocarbon habitat of the ‘Arctic Alaska Microplate’. *Marine and Petroleum Geology*, 4, 2-34. doi: 10.1016/0264-8172(87)90019-5
- Hyndman, R. D., Currie, C. A., & Mazzotti, S. P. (2005). Subduction zone backarcs, mobile belts, and orogenic heat. *Geological Society of America Today*, 15(23). doi: 10:1130/1052-5173
- Jadamec, M. A., & Billen, M. I. (2010). Reconciling surface plate motions and rapid three-dimensional flow around a slab edge. *Nature*, 465, 338-342.
- Jadamec, M. A., & Billen, M. I. (2012). The role of rheology and slab shape on rapid mantle flow: Three-dimensional numerical models of the Alaska slab edge. *Journal of Geophysical Research: Solid Earth*, 117, 1-20. doi: 10.1029/2011JB008563
- Jadamec, M. A., Billen, M. I., & Roeske, S. M. (2013). Three-dimensional numerical models of flat slab subduction and the Denali fault driving deformation in south-central Alaska. *Earth and Planetary Science Letters*, 376, 29-42. Retrieved from <http://dx.doi.org/10.1016/j.epsl.2013.06.009> doi: 10.1016/j.epsl.2013.06.009
- Jiang, C., Schmandt, B., Ward, K. M., Lin, F., & Worthington, L. L. (2018, 10). Upper mantle seismic structure of Alaska from Rayleigh and S wave tomography. *Geophysical Research Letters*, 45, 10,350-10,359. Retrieved from <https://onlinelibrary.wiley.com/doi/10.1029/2018GL079406> doi: 10.1029/2018GL079406
- Jones, P. B. (1980). Evidence from Canada and Alaska on plate tectonic evolution of the Arctic Ocean Basin. *Nature*, 285, 215-217. Retrieved from <https://www.nature.com/articles/285215a0> doi: 10.1038/285215a0
- Kalbas, J. L., Freed, A. M., & Ridgway, K. D. (2008). Contemporary fault mechanics in southern Alaska. *Geophysical Monograph Series*, 179, 321–336.
- Kim, Y., Abers, G. A., Li, J., Christensen, D., Calkins, J., & Rondenay, S. (2014, 3). Alaska Megathrust 2: Imaging the megathrust zone and Yakutat/Pacific plate interface in the Alaska subduction zone. *Journal of Geophysical Research: Solid Earth*, 119, 1924-1941. Retrieved from <https://onlinelibrary.wiley.com/doi/full/10.1002/2013JB010581> doi: 10.1002/2013JB010581
- Koehler, R., & Carver, G. (2018, 5). Active faults and seismic hazards in Alaska. In *Alaska Division of Geological and Geophysical Surveys Miscellaneous Publication* (Vol. 160, p. 59p). doi: 10.14509/29705
- Koons, P. O., Hooks, B. P., Pavlis, T., Upton, P., & Barker, A. D. (2010, 8). Three-dimensional mechanics of Yakutat convergence in the southern Alaskan plate corner. *Tectonics*, 29. Retrieved from <https://agupubs.onlinelibrary.wiley.com/doi/10.1029/2009TC002463> doi: 10.1029/2009TC002463
- Lahr, J. C., & Plafker, G. (1980). Holocene Pacific-North American plate interaction in southern Alaska: implications for the Yakataga seismic gap. *Geology*, 8, 483-486.
- Langston, C. A. (1977, 6). Corvallis, Oregon, crustal and upper mantle receiver structure from teleseismic p and s waves. *Bulletin of the Seismological Society of America*, 67, 713-724. doi: 10.1785/BSSA0670030713

- 1140 Lekic, V., & Romanowicz, B. (2011, 8). Tectonic regionalization without a priori information:
 1141 A cluster analysis of upper mantle tomography. *Earth and Planetary Science Letters*, *308*, 151-160. doi: 10.1016/J.EPSL.2011.05.050
 1142
- 1143 Liu, C., Zhang, S., Sheehan, A. F., & Ritzwoller, M. H. (2022, 11). Surface wave isotropic
 1144 and azimuthally anisotropic dispersion across Alaska and the Alaska-Aleutian subduc-
 1145 tion zone. *Journal of Geophysical Research: Solid Earth*, *127*, e2022JB024885. Re-
 1146 trieval from <https://onlinelibrary.wiley.com/doi/10.1029/2022JB024885> doi:
 1147 10.1029/2022JB024885
- 1148 Mann, M. E., Abers, G. A., Daly, K. A., & Christensen, D. H. (2022, 1). Subduction of
 1149 an oceanic plateau across southcentral Alaska: Scattered-wave imaging. *Journal of*
 1150 *Geophysical Research: Solid Earth*, *127*. doi: 10.1029/2021JB022697
 1151 Martin-Short, R., Allen, R., Bastow, I. D., Porritt, R. W., & Miller, M. S. (2018,
 1152 11). Seismic imaging of the Alaska subduction zone: Implications for slab geom-
 1153 etry and volcanism. *Geochemistry, Geophysics, Geosystems*, *19*, 4541-4560. Re-
 1154 trieval from <https://onlinelibrary.wiley.com/doi/10.1029/2018GC007962> doi:
 1155 10.1029/2018GC007962
- 1156 McConeghy, J., Flesch, L., & Elliott, J. (2022, 10). Investigating the effect of man-
 1157 tle flow and viscosity structure on surface velocities in Alaska using 3-D geody-
 1158 namic models. *Journal of Geophysical Research: Solid Earth*, *127*. Retrieved from
 1159 <https://onlinelibrary.wiley.com/doi/10.1029/2022JB024704> doi: 10.1029/
 1160 2022JB024704
- 1161 Miller, M. S., & Moresi, L. (2018, 11). Mapping the alaskan moho. *Seismological Research*
 1162 *Letters*, *89*, 2430-2436. doi: 10.1785/0220180222
 1163 Miller, M. S., O'Driscoll, L. J., Porritt, R. W., & Roeske, S. M. (2018). Multiscale crustal
 1164 architecture of Alaska inferred from p receiver functions. *Lithosphere*, *10*, 267-278.
 1165 doi: 10.1130/L701.1
 1166 Molnar, P., & Dayem, K. E. (2010, 8). Major intracontinental strike-slip faults
 1167 and contrasts in lithospheric strength. *Geosphere*, *6*, 444-467. Retrieved
 1168 from <http://pubs.geoscienceworld.org/gsa/geosphere/article-pdf/6/4/444/3338959/444.pdf> doi: 10.1130/GES00519.1
 1169
- 1170 Moore, T. E., & Box, S. E. (2016). Age, distribution and style of deformation in Alaska
 1171 north of 60° n: Implications for assembly of Alaska. *Tectonophysics*, *691*, 133–170.
 1172 Moresi, L., Betts, P., Miller, M., & Cayley, R. (2014). Dynamics of continental accretion.
 1173 *Nature*, *508*(7495), 245–248.
 1174 Mukasa, S. B., Andronikov, A. V., & Hall, C. M. (2007). The 40Ar/39Ar chronol-
 1175 ogy and eruption rates of Cenozoic volcanism in the eastern Bering Sea Vol-
 1176 canic Province, Alaska. *Journal of Geophysical Research: Solid Earth*, *112*(B6).
 1177 Retrieved from <https://agupubs.onlinelibrary.wiley.com/doi/abs/10.1029/2006JB004452> doi: <https://doi.org/10.1029/2006JB004452>
 1178
- 1179 Müller, R. D., Zahirovic, S., Williams, S. E., Cannon, J., Seton, M., Bower, D. J., ...
 1180 Gurnis, M. (2019). A global plate model including lithospheric deformation along
 1181 major rifts and orogens since the Triassic. *Tectonics*, *38*(6), 1884–1907.
 1182 Nayak, A., Eberhart-Phillips, D., Ruppert, N. A., Fang, H., Moore, M. M., Tape, C., ...
 1183 Thurber, C. H. (2020, 11). 3D seismic velocity models for Alaska from joint tomo-
 1184 graphic inversion of body-wave and surface-wave data. *Seismological Research*
 1185 *Letters*, *91*, 3106-3119. Retrieved from <http://pubs.geoscienceworld.org/ssa/srl/article-pdf/91/6/3106/5176960/srl-2020214.1.pdf> doi: 10.1785/0220200214
 1186
- 1187 Nokleberg, W., Aleinikoff, J., Bundtzen, T., & Hanshaw, M. (2013). *Geologic strip map*
 1188 *along the Hines Creek Fault showing evidence for Cenozoic displacement in the west-*
 1189 *ern Mount Hayes and northeastern Healy quadrangles, eastern Alaska Range, Alaska*
 1190 *(Tech. Rep.).* Retrieved from <https://pubs.usgs.gov/sim/3238/>
- 1191 Nokleberg, W. J., MollStalcup, E., Miller, T., Brew, D., Grantz, A., Reed Jr, J., ... Pat-
 1192 ton Jr, W. W. (1994). *Tectonostratigraphic terrane and overlap assemblage map of*
 1193 *Alaska.* US Geological Survey, Open-File Report 94-194.
 1194 O'Driscoll, L. J., & Miller, M. S. (2015, 4). Lithospheric discontinuity structure in Alaska,

- thickness variations determined by sp receiver functions. *Tectonics*, 34, 694-714. doi: 10.1002/2014TC003669
- Pavlis, G. L., Bauer, M. A., Elliott, J. L., Koons, P., Pavlis, T. L., Ruppert, N., ... Worthington, L. L. (2019). A unified three-dimensional model of the lithospheric structure at the subduction corner in southeast Alaska: Summary results from steep. *Geosphere*, 15, 382-406. doi: 10.1130/GES01488.1
- Pavlis, T. L., Amato, J. M., Trop, J. M., Ridgway, K. D., Roeske, S. M., & Gehrels, G. E. (2019). Subduction polarity in ancient arcs; a call to integrate geology and geophysics to decipher the Mesozoic tectonic history of the Northern Cordillera of North America. *GSA Today*, 29(11), 4 - 10.
- Plafker, G., & Berg, H. C. (1994, 4). Overview of the geology and tectonic evolution of Alaska. In (p. 989-1021). Geological Society of America. Retrieved from <https://pubs.geoscienceworld.org/books/book/875/chapter/4867358/> doi: 10.1130/DNAG-GNA-G1.989
- Plafker, G., Gilpin, L. M., & Lahr, J. C. (1994). Plate 12: Neotectonic Map of Alaska. In G. Plafker & H. Berg (Eds.), *The geology of north america* (Vols. G1, The Geology of Alaska). Boulder, Colo.: Geological Society of America.
- Plafker, G., Hudson, T., Bruns, T., & Rubin, M. (1978). Late Quaternary offsets along the Fairweather fault and crustal plate interactions in southern Alaska. *Canadian Journal of Earth Sciences*, 15(5), 805-816. Retrieved from <https://doi.org/10.1139/e78-085> doi: 10.1139/e78-085
- Plafker, G., Moore, J. C., & Winkler, G. R. (1994). Geology of the southern Alaska margin. In G. Plafker & H. Berg (Eds.), *The geology of north america* (Vols. G1, The Geology of Alaska, p. 389-449). Boulder, Colo.: Geological Society of America.
- Rondenay, S., Abbers, G. A., & van Keken, P. E. (2008, 4). Seismic imaging of subduction zone metamorphism. *Geology*, 36, 275-278. doi: 10.1130/G24112A.1
- Rondenay, S., Montési, L. G., & Abbers, G. A. (2010, 8). New geophysical insight into the origin of the Denali volcanic gap. *Geophysical Journal International*, 182, 613-630. Retrieved from <https://academic.oup.com/gji/article/182/2/613/568363> doi: 10.1111/J.1365-246X.2010.04659.X
- Rossi, G., Abbers, G. A., Rondenay, S., & Christensen, D. H. (2006, 9). Unusual mantle poisson's ratio, subduction, and crustal structure in central Alaska. *Journal of Geophysical Research: Solid Earth*, 111, 9311. Retrieved from <https://onlinelibrary.wiley.com/doi/full/10.1029/2005JB003956> doi: 10.1029/2005JB003956
- Ruppert, N. A., & West, M. E. (2020, 3). The impact of USArray on earthquake monitoring in Alaska. *Seismological Research Letters*, 91, 601-610. doi: 10.1785/0220190227
- Schaeffer, A. J., & Lebedev, S. (2015, 1). Global heterogeneity of the lithosphere and underlying mantle: A seismological appraisal based on multimode surface-wave dispersion analysis, shear-velocity tomography, and tectonic regionalization. *The Earth's Heterogeneous Mantle: A Geophysical, Geodynamical, and Geochemical Perspective*, 3-46. Retrieved from https://link.springer.com/chapter/10.1007/978-3-319-15627-9_1 FIGURES/19 doi: 10.1007/978-3-319-15627-9_1/FIGURES/19
- Schulte-Pelkum, V., Caine, J. S., Jones, J. V., & Becker, T. W. (2020, 11). Imaging the tectonic grain of the Northern Cordillera Orogen using Transportable Array receiver functions. *Seismological Research Letters*, 91, 3086-3105. doi: 10.1785/0220200182
- Searcy, C. K., Christensen, D. H., & Zandt, G. (1996, 2). Velocity structure beneath college station Alaska from receiver functions. *Bulletin of the Seismological Society of America*, 86, 232-241. doi: 10.1785/BSSA08601A0232
- Seton, M., Müller, R. D., Zahirovic, S., Williams, S., Wright, N. M., Cannon, J., ... McGirr, R. (2020). A global data set of present-day oceanic crustal age and seafloor spreading parameters. *Geochemistry, Geophysics, Geosystems*, 21(10), e2020GC009214.
- Sharples, W., Jadamec, M. A., Moresi, L. N., & Capitanio, F. (2014). Overriding plate controls on subduction evolution. *Journal of Geophysical Research*, 119, 6684-6704. doi: 10.1002/2014JB011163
- Silberling, N. J., Jones, D. L., Monger, J. W. H., Coney, P. J., Berg, H. C., & Plafker, G.

- 1250 (1994). Plate 3: Lithotectonic terrane map of Alaska and adjacent parts of Canada. In
 1251 G. Plafker & H. Berg (Eds.), *The Geology of North America* (Vols. G1, The Geology
 1252 of Alaska). Boulder, Colo.: Geological Society of America.
- 1253 Strauss, J. V., Macdonald, F. A., Taylor, J. F., Repetski, J. E., & McClelland, W. C.
 1254 (2013). Laurentian origin for the North Slope of Alaska: Implications for the tectonic
 1255 evolution of the arctic. *Lithosphere*, 5, 477-482. doi: 10.1130/L284.1
- 1256 Tavenard, R., Faouzi, J., Vandewiele, G., Divo, F., Androz, G., Holtz, C., ... Woods,
 1257 E. (2020). Tslearn, A Machine Learning Toolkit for Time Series Data. *Journal of
 1258 Machine Learning Research*, 21(118), 1-6. Retrieved from <http://jmlr.org/papers/v21/20-091.html>
- 1259 Torne, M., Jimenez-Munt, I., Verges, J., Fernandez, M., Carballo, A., & Jadamec, M. A.
 1260 (2019). Regional crustal and lithospheric thickness model for Alaska, the Chukchi
 1261 Shelf, and the inner and outer Bering Shelves. *Geophysical Journal International*,
 1262 *ggz424*. doi: <https://doi.org/10.1093/gji/ggz424>
- 1263 Tozer, B., Sandwell, D. T., Smith, W. H., Olson, C., Beale, J., & Wessel, P. (2019). Global
 1264 bathymetry and topography at 15 arc sec: Srtm15+. *Earth and Space Science*, 6(10),
 1265 1847-1864.
- 1266 Veenstra, E., Christensen, D. H., Abbers, G. A., & Ferris, A. (2006, 9). Crustal thickness
 1267 variation in south-central Alaska. *Geology*, 34, 781-784. doi: 10.1130/G22615.1
- 1268 von Gosen, W., Piepjohn, K., McClelland, W., & Colpron, M. (2019, 6). Evidence for
 1269 the sinistral Porcupine shear zone in North Yukon (Canadian Arctic) and geotectonic
 1270 implications. In (p. 473-491). Geological Society of America. doi: 10.1130/2019
 1271 .2541(21)
- 1272 Ward, K. M., & Lin, F. C. (2018). Lithospheric structure across the Alaskan cordillera from
 1273 the joint inversion of surface waves and receiver functions. *Journal of Geophysical
 1274 Research: Solid Earth*, 123, 8780-8797. doi: 10.1029/2018JB015967
- 1275 Wessel, P., Luis, J. F., Uieda, L., Scharroo, R., Wobbe, F., Smith, W. H. F., & Tian,
 1276 D. (2019, 11). The Generic Mapping Tools Version 6. *Geochemistry, Geophysics,
 1277 Geosystems*, 20, 5556-5564. doi: 10.1029/2019GC008515
- 1278 Woppard, G. P., Ostenso, N. A., Thiel, E., & Bonini, W. E. (1960, 3). Gravity anomalies,
 1279 crustal structure, and geology in Alaska. *Journal of Geophysical Research*, 65, 1021-
 1280 1037. Retrieved from <http://doi.wiley.com/10.1029/JZ065i003p01021> doi: 10
 1281 .1029/JZ065i003p01021
- 1282 Yang, X., Bryan, J., Okubo, K., Jiang, C., Clements, T., & Denolle, M. A. (2022b, 11). Optimal
 1283 stacking of noise cross-correlation functions. *Geophysical Journal International*,
 1284 232, 1600-1618. Retrieved from <https://academic.oup.com/gji/article/232/3/1600/6762921> doi: 10.1093/gji/ggac410
- 1285 Yang, X., & Gao, H. (2020, 11). Segmentation of the Aleutian-Alaska subduction zone
 1286 revealed by full-wave ambient noise tomography: Implications for the along-strike
 1287 variation of volcanism. *Journal of Geophysical Research: Solid Earth*, 125, 1-20. Re-
 1288 tried from <https://onlinelibrary.wiley.com/doi/10.1029/2020JB019677> doi:
 1289 10.1029/2020JB019677
- 1290 Yang, X., Zuffoletti, I. D., D'Souza, N. J., & Denolle, M. A. (2022a, 1). *SeisGo: A ready-to-
 1291 go Python toolbox for seismic data analysis* [Computer Software]. Zenodo. Retrieved
 1292 from <https://doi.org/10.5281/zenodo.5873724> doi: 10.5281/zenodo.5873724
- 1293 Zhang, Y., Li, A., & Hu, H. (2019). Crustal structure in Alaska from receiver function
 1294 analysis. *Geophysical Research Letters*, 46, 1284-1292. doi: 10.1029/2018GL081011
- 1295